LEVEL II

TECHNICAL REPORT ARBRL-TR-02069

IMPACT MODELS FOR PENETRATION AND HOLE GROWTH

William P. Walters
John N. Majerus

May 1978

US ARMY ARMAMENT RESEARCH AND DEVELOPMENT COMMAND
BALLISTIC RESEARCH LABORATORY
ABERDEEN PROVING GROUND, MARYLAND

Destroy this report when it is no longer needed.
Do not return it to the originator.

Secondary distribution of this report by originating or sponsoring activity is prohibited.

Additional copies of this report may be obtained from the National Technical Information Service, U.S. Department of Commerce, Springfield, Virginia 22161.

The findings in this report are not to be construed as an official Department of the Army position, unless so designated by other authorized documents.

The use of trade names or manufacturers' names in this report does not constitute indorsement of any commercial product.

UNCLASSIFIED

SECURITY CLASSIFICATION OF THIS PAGE (When Data Entered)

REPORT DOCUMENTATION PAGE

READ INSTRUCTIONS BEFORE COMPLETING FORM

1. REPORT NUMBER: TECHNICAL REPORT ARBRL-TR-02069
2. GOVT ACCESSION NO.
3. RECIPIENT'S CATALOG NUMBER

4. TITLE (and Subtitle): IMPACT MODELS FOR PENETRATION AND HOLE GROWTH
5. TYPE OF REPORT & PERIOD COVERED: Final
6. PERFORMING ORG. REPORT NUMBER

7. AUTHOR(s): William P. Walters, John N. Majerus
8. CONTRACT OR GRANT NUMBER(s)

9. PERFORMING ORGANIZATION NAME AND ADDRESS: U.S. Army Ballistic Research Laboratory (ATTN: DRDAR-BLT) Aberdeen Proving Ground, MD 21005
10. PROGRAM ELEMENT, PROJECT, TASK AREA & WORK UNIT NUMBERS: RDT&E 1L662618AH80

11. CONTROLLING OFFICE NAME AND ADDRESS: US Army Armament Research and Development Command, U.S. Army Ballistic Research Laboratory (ATTN: DRDAR-BL) Aberdeen Proving Ground, MD 21005
12. REPORT DATE: MAY 1978
13. NUMBER OF PAGES: 59

14. MONITORING AGENCY NAME & ADDRESS (if different from Controlling Office)
15. SECURITY CLASS. (of this report): UNCLASSIFIED
15a. DECLASSIFICATION/DOWNGRADING SCHEDULE

16. DISTRIBUTION STATEMENT (of this Report)

Approved for public release; distribution unlimited.

DDC RECEIVED JUL 18 1978 B

17. DISTRIBUTION STATEMENT (of the abstract entered in Block 20, if different from Report)

SET 1 AD-A

18. SUPPLEMENTARY NOTES

19. KEY WORDS (Continue on reverse side if necessary and identify by block number)

Warhead
Shaped-Charge Jet
KE Penetrator
penetration
hole profile
jet-target interaction
modeling

20. ABSTRACT (Continue on reverse side if necessary and identify by block number) (mba)

Given a hit and specific target, the target's vulnerability depends upon the type of threat, for example, kinetic energy (KE) penetrator, shaped-charge jet or high explosive. This report addresses the threats associated with KE rod penetrators and shaped-charge jets. The questions studied are penetration capability, decreasing penetrator velocity and mass through the armor, hole-growth rate and hole size. The model is based on the conservation of mass and the equations of motion in both the radial and axial directions and is used to

(continued)

DD FORM 1 JAN 73 1473 EDITION OF 1 NOV 65 IS OBSOLETE

UNCLASSIFIED

(Item 20 Continued)

predict the time dependent penetration depth, penetration velocity, radial velocity imparted to the target, target hole profile, and the erosion of the penetrating projectile. Incompressible flow is assumed for the axial flow, but target-strength effects and viscous-shear effects are included in the analysis. Plugging of the target is not considered in the present model and all target flow is assumed to occur in the radial direction. This radial flow (compressible but uniform) is assumed to occur in three different regimes: first, target material under the interface flows radially outwards (primary regime), then, eroded penetrator forces additional radial flow of target material (secondary regime), and finally, the radial inertia induced by primary and secondary flow is absorbed by the surrounding target material (tertiary regime). Due to various assumptions, the axial and radial flows are uncoupled, and the radial flow can be obtained once the penetration and penetrator velocities are determined. Several special cases of axial flow are considered and compare well with a variety of experimental data. Special cases of radial flow will be considered in a future report.

TABLE OF CONTENTS

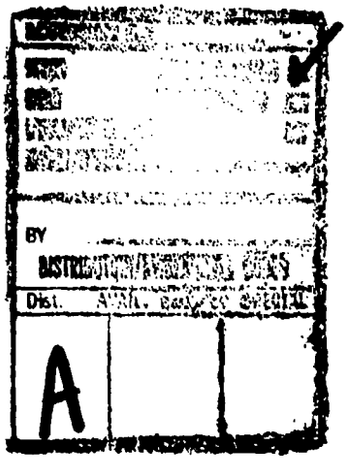

LIST OF ILLUSTRATIONS

I. INTRODUCTION

Numerous penetration models have been developed in the past, and a large number of these and the corresponding experimental data can be found in References 1 through 14. The experimental data show that

---

[1] *E. M. Pugh, and E. L. Fireman, "Fundamentals of Jet Penetration," Carnegie Institute of Technology, Monthly Report OTB-4 (OSRD-4357), November, 1944.*

[2] *R. J. Eichelberger, "Re-examination of the Theories of Jet Formation and Target Penetration by Lined Cavity Charges," Carnegie Institute of Technology, CEL Report No. 1, June, 1954.*

[3] *R. DiPersio, J. Simon, and A. Merendino, "Penetration of Shaped-Charge Jets Into Metallic Targets," BRL Report No. 1296, September 1965.* (AD #476717)

[4] *F. Allison and R. Vitali, "A New Method of Computing Penetration Variables for Shaped-Charge Jets," BRL Report No. 1184, January, 1963.* (AD #400485)

[5] *A. Merendino and R. Vitali, "The Penetration of Shaped Charge Jets Into Steel and Aluminum Targets of Various Strengths (U)," BRL Memorandum Report No. 1932 (CLASSIFIED), August, 1968.* (AD #392672)

[6] *R. DiPersio and J. Simon, "Resistance of Solid Homogeneous Targets to Shaped Charge Jet Penetration," Ballistic Research Laboratories Report No. 1417, October 1968.* (AD #841804)

[7] *Hypervelocity Impact Symposium Proceedings, Fourth Symposium, Vols. I - III, Air Proving Ground Center, Eglin Air Force Base, September 1960.*

[8] *M. Defourneaux, "Examination of the Theories Dealing with The Penetration of A Projectile into a Plastic Material," U.S. Army Foreign Science and Technology Center, FSTC-HT-23-1794-72, 13 March 1973.*

[9] *D. R. Christman and J. W. Gehring, "Semiannual Report on Penetration Mechanisms of High-Velocity Projectiles," General Motors Report TR63-250, 31 December 1963.*

[10] *W. Johnson, Impact Strength of Materials, Edward Arnold, London, 1972, Chapter 9.*

[11] *High-Velocity Impact Phenomena, Edited by R. Kinslow, Academic Press, 1970, Chap. IV, "Theory of Impact on Thin Targets and Shields and Correlation With Experiment," By J. W. Gehring, Jr., and Chap. IX "Engineering Considerations in Hypervelocity Impact," by J.W. Gehring, Jr.*

[12] *G. Weihrauch, "The Behavior of Copper Pins Upon Impacting Various Materials at Velocities of 50 - 1640 m/s," FSTC-HT-23-0004-74, 10 September 1973.*

[13] *A. Tate, "A Theory for the Deceleration of Long Rods After Impact," J. Mech. Phys. Solids, Vol. 15, 1967.*

[14] *W. A. Allen, E. B. Mayfield, and H. L. Morrison, "Dynamics of a Projectile Penetrating Sand," J. of Applied Physics, Vol. 28, No. 3, March, 1957.*

strength effects are important for both KE penetrators[7,9] and shaped-charge jets[2,5,6] and several of the above models have included target-strength effects. However, the majority of these models assume that strength effects are small compared to the effects of impact velocity and hence consider density as the predominant target parameter. Also, separate models have been developed for the penetration behavior of shaped-charge jets versus KE penetrators and different theories exist for the two types of penetrators. Furthermore, predictive models are lacking for the mass and velocity of frontal ejecta, radial hole growth, hole contour, radial velocity induced into the penetrator at the penetrator-target interface and the residual mass and velocity of a rod penetrator. The model introduced in this report is applicable to both jets and rod penetrators, attempts to provide predictive models which are currently lacking, and includes the effects of both strength and viscosity of the target.

II. FORMULATION AND DERIVATION OF THE MODEL

The intent of this model is to increase the accuracy obtained from earlier models (References 1 - 3, 7 and 9), as well as to extend the amount of information derivable from simple models. In an earlier approach, the authors[15] derived an approximate model which relaxed to known solutions for shaped-charge jets and penetrators, and included strength and viscosity effects. However, the radial flow of target material could not be evaluated. In the current model, both axial and radial flow of the target are considered by employing conservation of mass and momentum sequentially to the axial and radial directions.

There are several ways in which to apply the conservation laws to the penetration problem. In the differential approach, the equations are expressed in terms of unknown stresses, displacement and velocity fields. This would yield partial differential equations analogous to (although possibly simpler than) those used in existing hydrodynamic codes. However, the usage of such codes for a vulnerability study would be prohibitive in both time and cost. Conversely, a closed-form solution would be readily adaptable to a vulnerability analysis, and inspection of the variables contained within the solution would provide insight into ways of either enhancing or reducing target vulnerability (given a hit). Therefore, in an attempt to obtain a closed-form solution, an integral approach was taken to the problem.

The integral approach involves approximating the real problem by a series of regions, in each of which the internal fields are assumed to be constant and whose boundaries are acted upon by some average surface-traction at the centroid of the surface. These regions will be referred

[15] *W. P. Walters and J. N. Majerus, "Hypervelocity Impact Models for Hole Growth and Geometry," Proceedings of the Third Annual Vulnerability/ Survivability Symposium ADPA, Naval Amphibious Base, Coronada, CA, 1977.*

to as free-body regions. Applying this approach to the penetrator problem, the mixing of the penetrator and target materials in the interaction region and the convective momentum-flux terms (spatial gradients of the velocity) are ignored. This approach serves to partially decouple the governing equations and results in a system of ordinary differential equations with respect to time.

To apply this approach to the penetrator problem, we first need to establish a global free-body which relates the penetrator/target interface location to an Eulerian reference plane. This establishes the penetration depth P with respect to the top of the target and defines the axial and radial velocities as dZ_{CG}/dt and dR_{CG}/dt, where R_{CG} and Z_{CG} are the center-of-mass coordinates. Figure 1 shows the penetrator at three global stages: initially when $t = t_o + \Delta t$, during penetration ($t > t_o + \Delta t$), and during free-flight at the same time t.

The top of Figure 1 shows the penetrator at some time Δt after impacting the target at time t_o. During this time Δt, the target material under the penetrator (to depth H) is replaced by penetrator material which has slowed down to a velocity U_o. This region of penetrator material of length H and of penetrator/target interface-velocity U is referred to as the interaction region. The details of the formation of this interaction region can only be obtained by elaborate hydrodynamic-code calculations[16,17] and are not considered in the present model.

Note that the time Δt is assumed to be small compared to the time t associated with penetration into the target, i.e., $t + \Delta t \approx t$. Also, the interaction height H is assumed to be small compared to either the thickness of the target or the penetrator-length ℓ_o. Flash radiography and hydrocode calculations[16,17] indicate that H is on the order of the penetrator radius for rod-type penetrators. Hence, the assumption on H should be valid except for problems involving extremely short penetrators or thin targets.

The second and third global stages are also indicated in Figure 1. The second stage refers to the projectile penetrating the material whereas the third stage (free-flight) is merely a reference stage required for stretching shaped-charge jets. The penetration P is referenced to the top of the target and the initial penetrator length is $\ell_o(t_o)$. For a shaped charge jet, $\ell_o(t_o) = Z_o(1 - V_I(t_o)/V_o)$ where V_o is the tip velocity, Z_o is the distance from the virtual origin[3,4],

---

[16] *W. E. Johnson, "Three-Dimensional Computations on Penetrator-Target Interactions," Ballistic Research Laboratory Contract Report No. 338, April 1977.* (AD #A041058)

[17] *V. Kucher, "Computer Study of the Effects of Rod Diameter and Target Thickness on the Penetration Process," Tech Report ARBRL-TR-02046, February, 1978.*

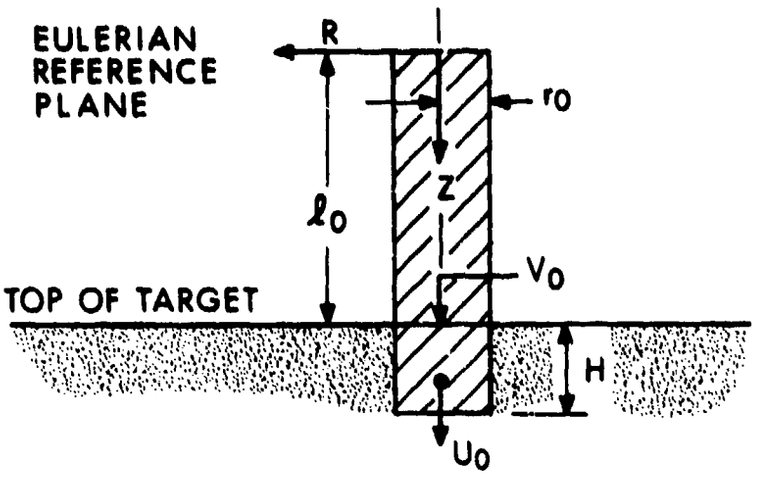

PENETRATOR AND INTERACTION
REGION AT TIME $(t_0 + \Delta t)$

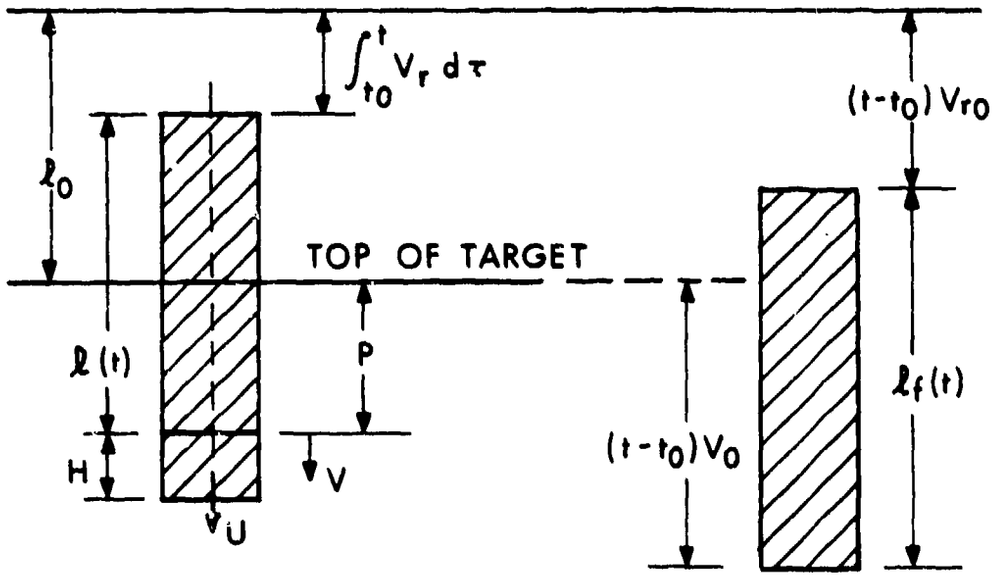

PENETRATOR AND INTERACTION
REGION AT TIME t

FREE FLIGHT PENETRATOR
AT TIME t

Figure 1. Global Penetrator Stages

and $V_r(t_o)$ is the velocity at the rear of the jet at the time of impact. Experiments and hydrocode calculations indicate that the value of V_r will not change during penetration until the penetrator/target interface approaches the rear of the jet. For a KE penetrator, $\ell_o(t_o)$ is the initial rod length and $V_r(t_o) = V_o$ at the time of impact. If the rod is decelerated during penetration, the value of V_r will change. However, V_r will be approximately equal to the velocity V at the top of the interaction region.

Based upon the configuration shown in Figure 1, the penetrator length $\ell(t)$ during penetration and the free-flight penetrator length $\ell_f(t)$ at the same time are respectively,

$$\ell(t) = \ell_o(t_o + \Delta t) - \Delta L + P - \int_{t_o+\Delta t}^{t} V_r(t)dt, \qquad (1)$$

$$\ell_f(t) = \ell_o(t_o + \Delta t) + (t - (t_o + \Delta t))(V_o - V_r(t_o + \Delta t), \qquad (2)$$

where ΔL is the length of penetrator lost during the formation of the interaction region. Also, conservation of mass of the free-flight penetrator requires that the rod radius r_j be

$$r_j^2(t) = r_o^2 \, (\ell_o(t_o) - \Delta L)/\ell_f(t) \qquad (3)$$

where r_o is r_j at $t = t_o + \Delta t$ and the penetrator is assumed to have the shape of a circular cylinder. Note that for a KE penetrator, $\ell_f(t) = \ell_o(t_o) - \Delta L$ and $r(t) = r_o(t)$ since $V_r(t_o) = V_o$ for free-flight.

Due to our assumptions concerning Δt and H, ΔL should be small compared to $\ell_o(t_o)$. Hence, $\ell_o(t_o) - \Delta L \sim \ell_o(t_o)$ and $t_o + \Delta t \sim t_o$. The penetrator's velocity V at the top of the interaction region is taken to be V_o at $t = t_o + \Delta t$, and the penetration depth P is referenced from the top of the interaction region.

Now that the global problem has been formulated, the corresponding free-bodies and localized flow associated with the interaction region must be established. The flows of target and penetrator materials are envisioned as occurring in two regimes. The first regime (regime A) involves a fixed amount of penetrator material contained within the interaction region, moving axially with velocity U, and displacing target material associated with depth H. The second regime (regime B)

involves additional penetrator material (due to the relative velocity V - U) flowing in and out of the interaction region. The penetrator flow out of the interaction region is accomplished by displacing target material located radially around the penetrator. Figure 2 shows schematic diagrams of the flow associated with these two regimes of flow.

In general, part of the target material under the interaction region may be compressed, and the remaining material flows in the radial and axial directions. The compressed target-material is either pushed ahead of the penetrator in the form of a so-called shear plug, or ejected from the back of the target in the form of debris. The target material in the radial region around the penetrator can flow in both the axial and radial directions. Similarly, the eroded penetrator mass (associated with the flow velocity V - U) can flow in both the radial and axial directions. However, if both penetrator and target materials flow in the axial and radial directions, a large number of coupled differential equations are required for solution. Furthermore, the partitioning of the mass flow under the interaction region is a complex phenomenon and may involve other analyses. Therefore, for the present investigation, the following assumptions are made concerning the regime A and B flows: all target material flows radially outwards under the interface during regime A, and during regime B the target and eroded penetrator materials flow only in the radial direction.

For axial flow the two penetrator regions are shown in Figure 3. In the present approach, the values of the penetrator's initial velocities (V_o and V_r), and size (r_o and ℓ_o), target density ρ_{To}, penetrator density ρ_o, target strength σ_T, penetrator strength σ, and target viscosity μ_T, and interaction viscosity μ are assumed to be known. The unknowns are the masses M_I and M_{II} of the two regions, the density ρ of the penetrator material in the interaction region, the height H of the interaction region, the velocity V_I of the penetrator material above the interaction region, the velocity V_r at the rear of the penetrator, the length ℓ of the penetrator, and the penetration depth P. The penetration velocity U is not an independent variable since it is related to penetration through the definition $U \equiv dP/dt$. Also, the radius r(t) and free-flight length $\ell_f(t)$ are considered known because of Equations (2) and (3). This gives eight unknowns and one equation (Equation 1). Hence seven more equations are needed.

Because of our definition of region II, $\frac{d}{dt}(M_{II}) \equiv 0$ and the following two equations apply:

$$M_{II} = \pi r_j^2 H\rho = \pi r^2(t_o)\, H(t_o)\, \rho_o \qquad (4)$$

whereas the mass of region I is

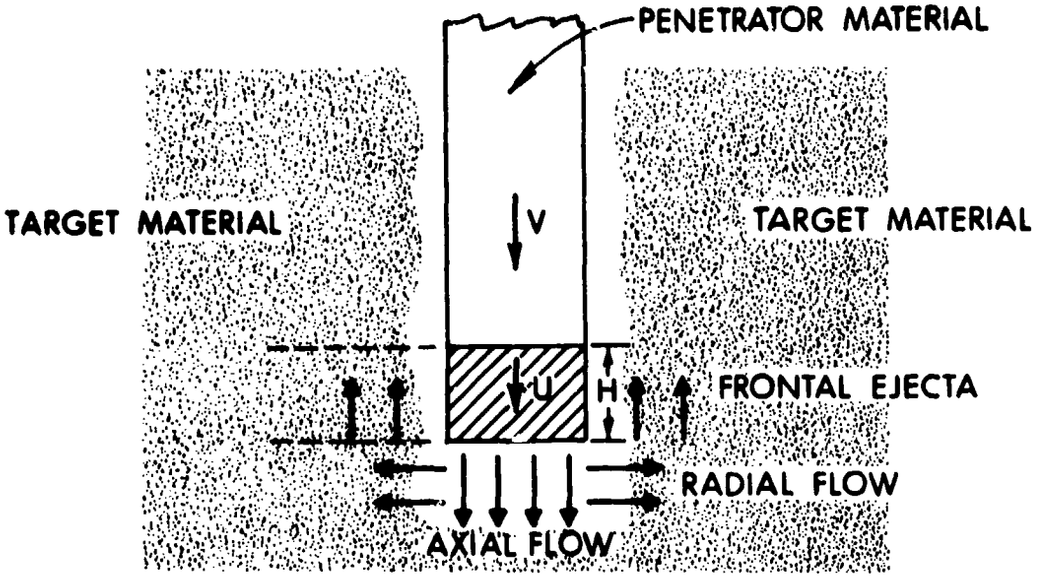

GENERAL TARGET AND PENETRATOR FLOWS FOR REGIME A

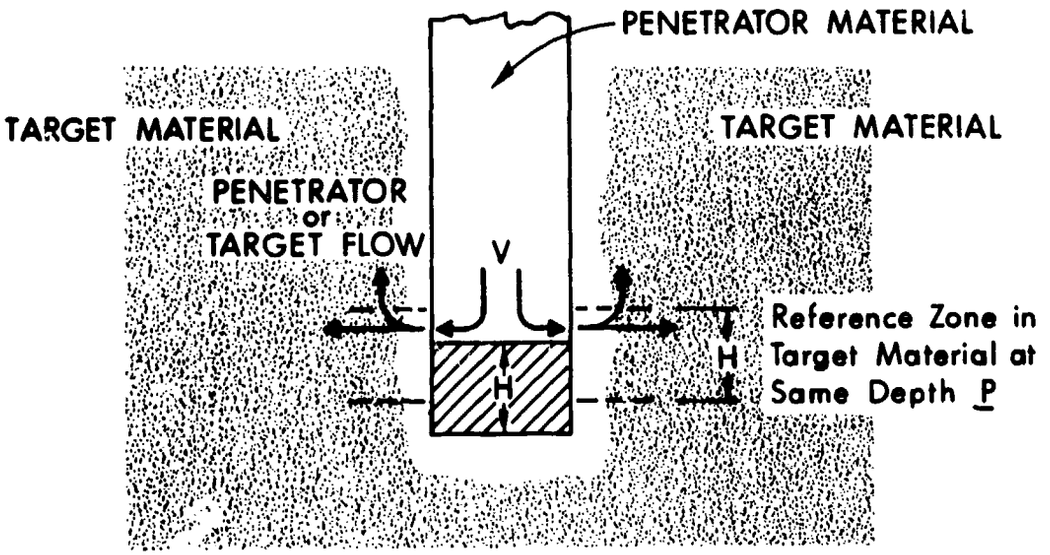

GENERAL TARGET AND PENETRATOR FLOWS FOR REGIME B

Figure 2. Schematic Diagrams of Penetrator and Target Flow

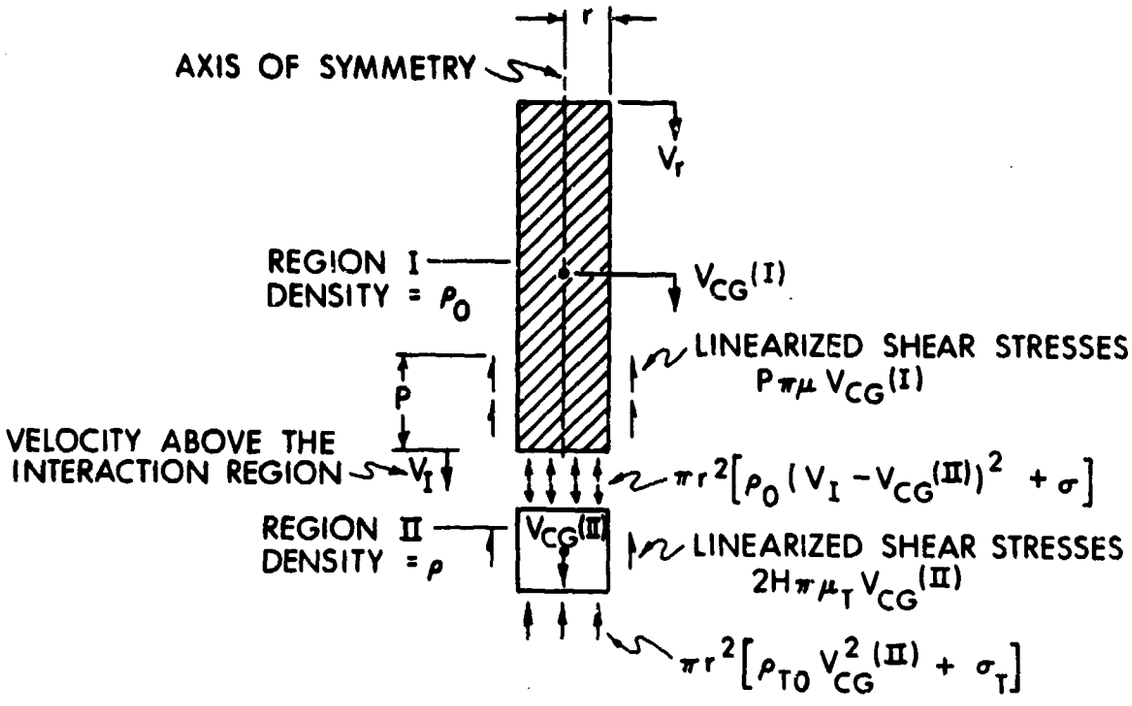

$$V_{CG}^{(I)} = \frac{d}{dt}\bar{z}_I$$

$$V_{CG}^{(III)} = \frac{d}{dt}(\ell_0 + P + H/2) = U + \frac{1}{2}\frac{dH}{dt}$$

Figure 3. Free-Body Configurations for Axial Flow

$$M_I = \pi r_j^2(t)\, \rho_o\, \ell(t). \tag{5}$$

Following the approach of Pugh, Fireman[1] and Eichelberger[2] for inertial resistance, equilibrium of axial momentum† for region II requires that

$$M_{II}(\dot{U} + \tfrac{1}{2}\ddot{H}) = \pi r_j^2\, (\sigma - \sigma_T) + \pi r_j^2 \rho_o\, (V_I - U)^2 - \pi r_j^2\, \rho_{To}\, U^2 - \pi H \mu_T\, 2U \tag{6}$$

where a superimposed dot denotes differentiation with respect to time and the flow shear-stresses are approximated as being associated with a linearized Newtonian-fluid. We now have five equations for the eight unknowns. Therefore, three additional relationships are required.

First, the height H will be assumed to be constant. This constant must be obtained either from radiographic observation, or hydrocode calculation[16,17], or may be considered in a parametric fashion. Two additional relationships involve two sets of assumptions made separately for jet and rod penetrators, i.e.,

$$V_r = V_{CG}(I) \quad \text{(rod)} \tag{7a}$$

$$V_r = V_{ro} \quad \text{(jet)} \tag{7b}$$

and

$$V_I = V_{CG}(I) \quad \text{(rod)} \tag{8a}$$

$$V_I = V_{ro} + (V_o - V_{ro})\ell/\ell_f \quad \text{(jet)} \tag{8b}$$

where $V_{CG}(I)$ = velocity at the center of gravity of the rod penetrator and $V_{ro} = V_r(t_o)$. The justification for Equations (7a), (7b) and (8a) were previously given. Equation (8b) corresponds to the assumption of a linear velocity-gradient in the jet. Radiographic observations[3] show that this is a good approximation for a variety of shaped-charges.

†*If not all of the eroded penetrator flows radially during regime B, then M_{II} changes with time and must be accounted for in Equation (6).*

Equations (7a) and (8a) introduce another unknown $V_{CG}(I)$ which can be related to the other variables through the conservation of axial momentum† applied to region I, i.e.,

$$\frac{d}{dt}(M_I\ V_{CG}(I)) = -\ \pi r_j^2[\rho_o(V_{CG}(I) - U)^2 + \sigma]$$
$$- \pi\ \mu\ P\ V_{CG}(I). \tag{9}$$

Therefore, the axial solution for shaped-charge jets involves Equations (1) through (8b) whereas KE penetrators require solving Equations (1) through (9).

Note that the height of the interaction region, H, need not always be assumed constant but could vary with time. One application would be a penetrator impacting a rigid (non-deforming) target where H = H(t) but the penetration is zero (see Reference 18). In this case the problem must be reformulated slightly with region II being attached to the top of the target, and mass M_{II} is no longer constant.

For radial flow during regimes A and B, axial views of the regions of interest are shown in Figures 4 and 5 respectively. The corresponding radial target-regions are denoted as regions III and IV respectively. These regions are of height H and located at depth P within the target. The penetrator/target interface reaches this depth at some time t_p. The radial extent of regions III and IV are denoted as R_o^* and R_o^{**} respectively.

During flow regime A, (see Figure 4), target material flows out from under the interface and compresses the target material contained within region III. The density ρ_T^* changes with time but is assumed to be uniform throughout region III. During flow regime A, the radial boundary R_o^* is assumed to be stationary. This flow regime lasts for time $t^* \equiv H/U$.

During flow regime B (see Figure 5), the eroded penetrator flows radially outwards and compresses the target material in region IV. The corresponding density ρ_T^{**} changes with time but is assumed to be uniform. The radial boundary R_o^{**} is assumed to be stationary and flow regime B lasts for a time t^*.

---

†*Appendix I lists a second approach for region I which is based upon a global momentum conservation equation where region II is viewed as a shock front with H → 0.*

[18]*M. Wilkins and M. Guinam, "Impact of Cylinders on a Rigid Boundary," J. of Appl. Phys., Vol. 44, No. 3, March 1973.*

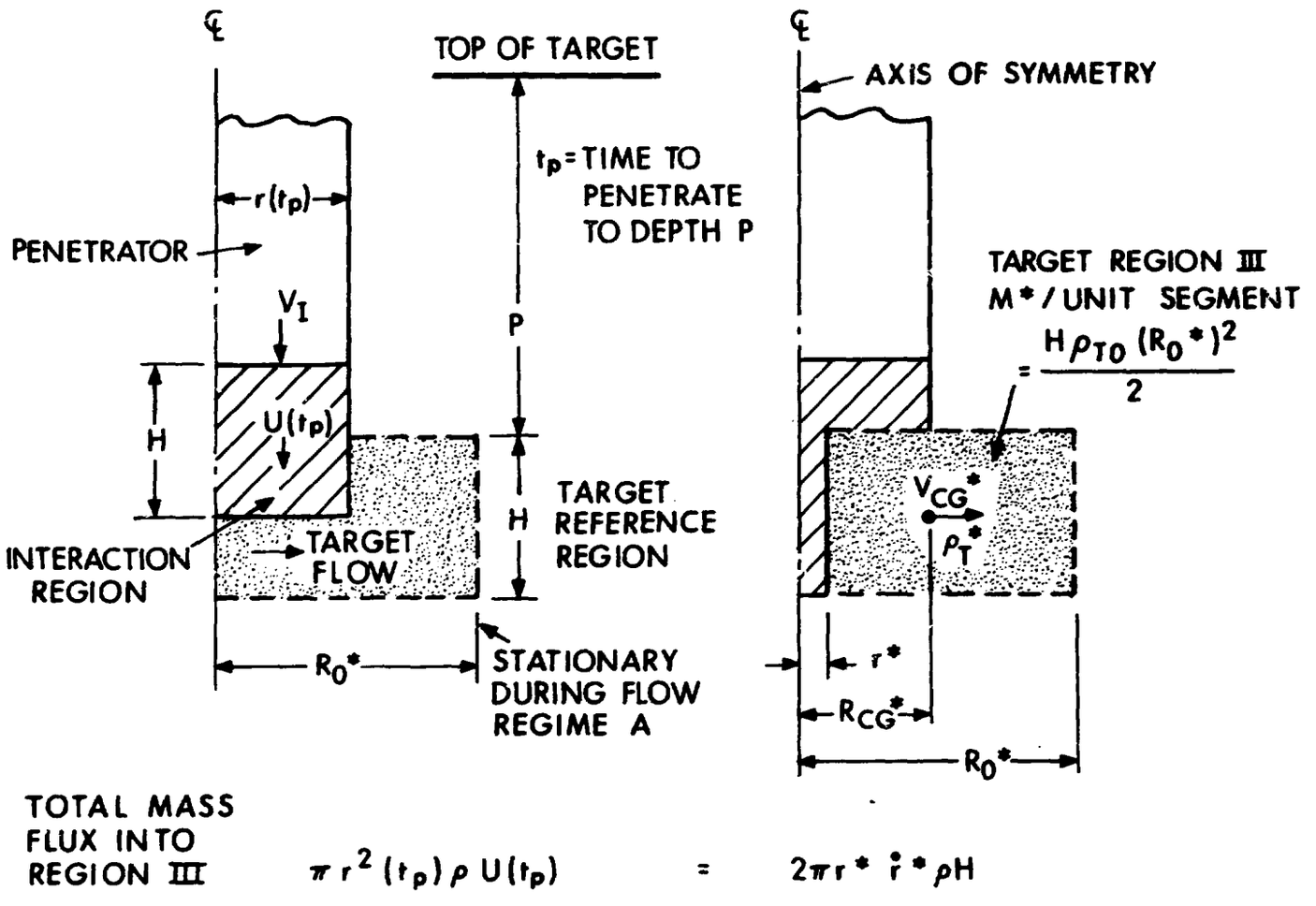

TOTAL MASS FLUX INTO REGION III $\quad \pi r^2(t_p)\, \rho\, U(t_p) = 2\pi r^* \dot{r}^* \rho H$

Figure 4. Two Axial Views of Radial Segment for Flow Regime A

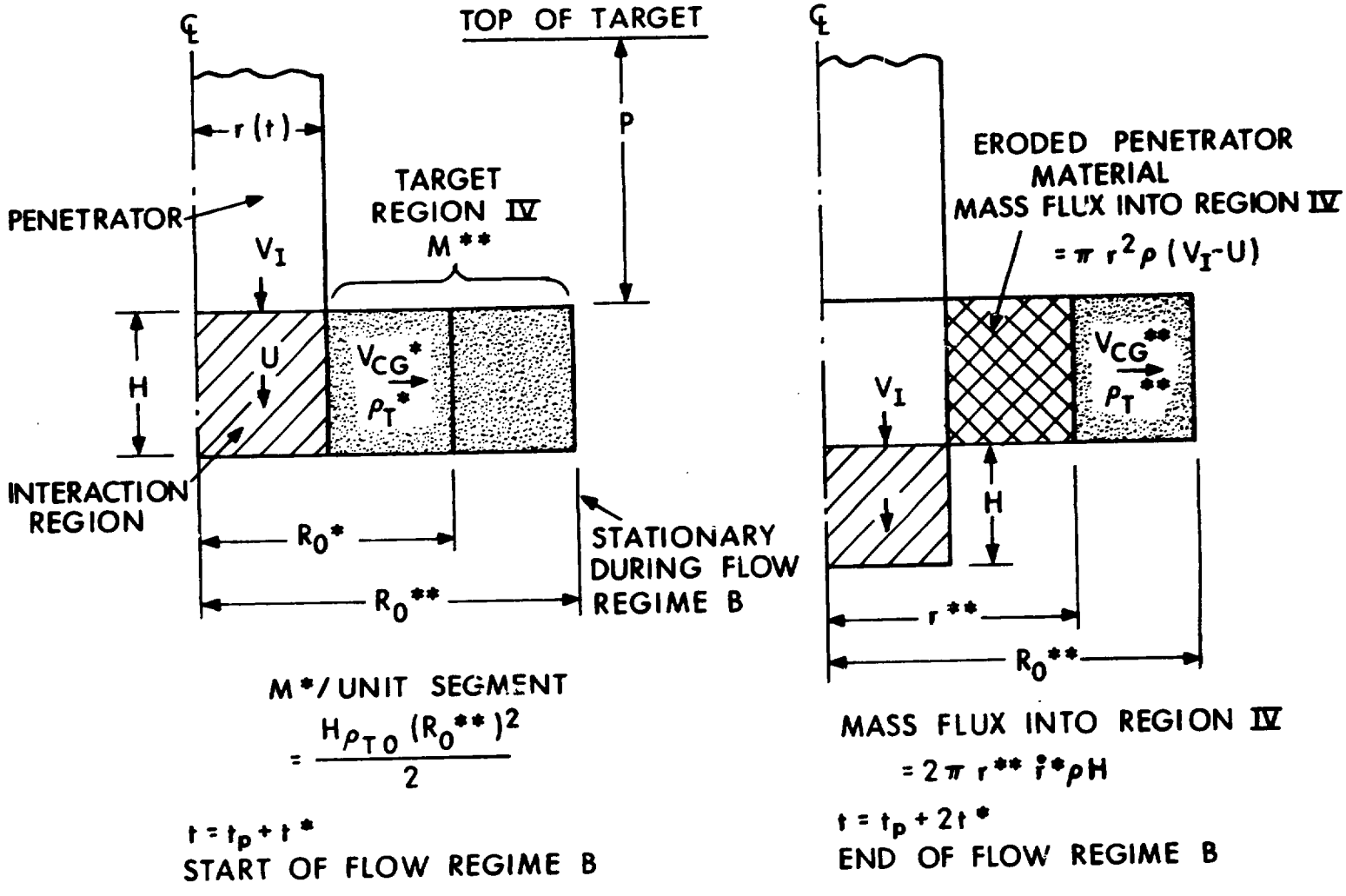

Figure 5. Axial Views of a Radial Segment for Flow Regime B at Two Different Times

There are six unknowns associated with each regime of flow, i.e., the regions III and IV. These unknowns are the following: the radial locations r^* and r^{**} of the penetrator/target interface, the radial locations R_o^* and R_o^{**} of the boundaries, the locations R_{CG}^* and R_{CG}^{**} and velocities V_{CG}^* and V_{CG}^{**} of the center-of-mass of the regions, and the masses M^* and M^{**} and densities ρ_T^* and ρ_T^{**} of the target material. Therefore, a total of 12 equations are required to solve for the regime A and B flows.

Eight equations can be obtained from the geometry and definition of regions III and IV,

$$M^*\Big|_{\substack{\text{unit}\\\text{segment}}} = H\,\rho_{To}(R_o^*)^2/2 \tag{10a}$$

$$M^{**}\Big|_{\substack{\text{unit}\\\text{segment}}} = H\,\rho_{To}(R_o^{**})^2/2 \tag{10b}$$

$$\rho_T^*[(R_o^*)^2 - (r^*)^2] = \rho_{To}(R_o^*)^2 \tag{11a}$$

$$\rho_T^{**}[(R_o^{**})^2 - (r^{**})^2] = \rho_{To}(R_o^{**})^2 \tag{11b}$$

$$V_{CG}^* = \dot{R}_{CG}^* \tag{12a}$$

$$V_{CG}^{**} = \dot{R}_{CG}^{**} \tag{12b}$$

$$R_{CG}^* = \frac{2}{3}\,\frac{[(R_o^*)^2 + r^*\,R_o^* + (r^*)^2]}{(R_o^* + r^*)} \tag{13a}$$

$$R_{CG}^{**} = \frac{2}{3}\,\frac{[(R_o^{**})^2 + r^{**}\,R_o^{**} + (r^{**})^2]}{(R_o^{**} + r^{**})} \tag{13b}$$

The equations for r^* and r^{**} stem from equating the axial penetrator-flux into the reference regions to the psuedo radial-fluxes (see Figures 4 and 5). This gives the following equations, for regions III and IV respectively,

$$r^* = \sqrt{(t - t_p)\, U\, r_o^2/H} \qquad \text{(rod)} \tag{14a}$$

$$= \sqrt{\frac{r_o^2\, \ell_o\, U}{H(V_o - V_{ro})}\, \ell n \left[\frac{\ell_o + (V_o - V_{ro})t}{\ell_o + (V_o - V_{ro})t_p}\right]} \qquad \text{(jet)} \tag{14b}$$

$$r^{**} = \sqrt{(t - t_{p1})(V - U)\, r_o^2/H} \qquad \text{(rod)} \tag{15a}$$

$$= \sqrt{\frac{r_o^2\, \ell_o\, (V - U)}{H(V_o - V_{ro})}\, \ell n \left[\frac{\ell_o + (V_o - V_{ro})t}{\ell_o + (V_o - V_{ro})t_{p1}}\right]} \qquad \text{(jet)} \tag{15b}$$

where $t_{p1} \equiv t_p + t^*$, Equations (14a) and (14b) are limited to the time interval $t_p \leq t \leq t_p + t^*$, and Equations (15a) and (15b) are limited to the interval $t_{p1} \leq t \leq t_{p1} + t^*$.

The last two equations deal with the conservation of radial momentum at various times during the flow regimes. For flow regime A, the instantaneous change of axial flow to radial flow at time $t = t_p$ introduces a mathematical singularity in the radial momentum equation, i.e., $\lim_{t \to t_p} \dot{r}^* \to \infty$. Therefore, for flow regime A, conservation of radial momentum will be applied only at the end of this flow regime, i.e., at $t = t_p + t^*$. Again, following the Pugh-Fireman-Eichelberger approach for inertial resistance, the balance of radial momentum yields,

$$M^* \dot{V}^*_{CG}\Big|_{t = t_p + t^*} = \Big\{ - R^*_o\, H\, [\sigma_T + (V^*_{CG})^2\, \rho_{To}]$$

$$- \mu_T\, [(R^*_o)^2 - (r^*)^2]\, V^*_{CG}/H \tag{16}$$

$$+ r^*\, H\, [\sigma + (V^*_{CG} - \dot{r}^*_{CG})^2 \rho_o] \Big\}_{t = t_p + t^*}$$

where $\dot{r}^{**}_{CG} = 2/3\ \dot{r}^{*}$ and the material's resistance is represented by a strength acting normal to the surfaces, and a linearized Newtonian shear-stress acting tangentially to the surfaces. Note that, because of Equations (10) through (15), the only unknown in Equation (16) is the radial location R^{*}_{o} which is constant at time $t = t_p + t^*$. Therefore, Equation (16) represents an algebraic equation (non-linear) for obtaining R^{*}_{o}.

The conservation of radial momentum is applied to region IV so that the change in momentum between times $t_p + t^*$ and $t_p + 2t^*$ equals the external forces acting over this time interval, i.e.,

$$\int_{t_p + t^*}^{t_p + 2t^*} d(MV) \equiv M^{**} V^{**}_{CG} (t_p + 2t^*) - M^{*} V^{*}_{CG} (t_p + t^*)$$

$$= \int_{t_p + t^*}^{t_p + 2t^*} \Big\{ - R^{**}_{o} H [\sigma_T + (V^{**}_{CG})^2 \rho_{To}] \qquad (17)$$

$$- \mu_T [(R^{**}_{o})^2 - (r^{**})^2] V^{**}_{CG}/H$$

$$+ r^{**} H [\sigma + (V^{**}_{CG} - \dot{r}^{**}_{CG})^2 \rho_o] \Big\} dt$$

where $\dot{r}^{**}_{CG} = 2/3\ \dot{r}^{**}$. Again, Equations (10) through (15) yield the time dependency for the integrand of Equation (17), and the solution to Equation (16) yields the value of M^* and V^{*}_{CG}. Hence, Equation (17) is an algebraic equation for the unknown constant R^{**}_{o}.

Figure 6 shows radial segments of target and penetrator materials as viewed at three different times. The top sketch refers to the target and penetrator materials at the end of flow regime A ($t = t_p + t^*$); the middle sketch corresponds to the materials at the end of flow regime B ($t = t_p + 2t^*$); and the bottom sketch views the materials at some time after the interaction region has passed. This latter stage of radial flow will be referred to as flow regime C. During this flow regime the outward flow for a unit segment of fixed target and penetrator masses are impeded by the target material remaining in the radial direction. The following 11 unknowns are associated with flow regime C: the constant masses M_p and M_T and time-dependent densities ρ and ρ_T of the penetrator and target materials, the radial location r_p of the penetrator material, the radial location R_I of the penetrator/target interface, the radial location R of the interface between the

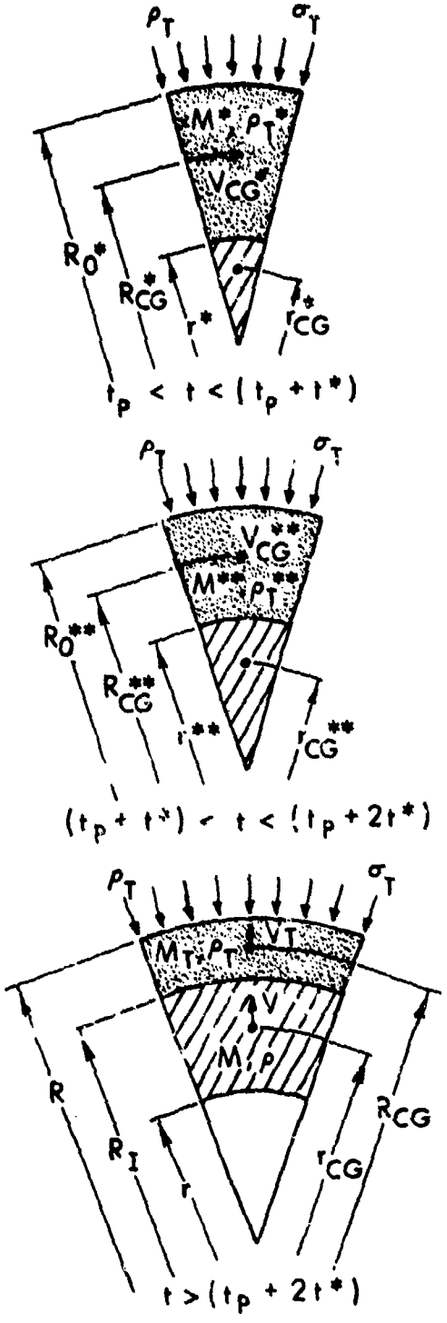

Figure 6. ..dial Views at Different Times for a Segme.. with Incremental Angular Width

moving and stationary target material, and lastly, the radial locations R_{CG} and r_{CG}, and respective velocities V_T and V_p, of the center-of-masses.

Based upon the geometry and definition of flow regime C, the following 8 equations can be applied,

$$M_T = (R_o^{**})^2 \, H \, \rho_{To}/2 \tag{18a}$$

$$M_p = (r^{**} \, (t_p + 2t^*))^2 H \, \rho_o/2 \tag{18b}$$

$$H \, \rho_T \, [R^2 - R_I^{\,2}] = M_T \tag{19a}$$

$$H \, \rho \, [R_I^{\,2} - r_p^{\,2}] = M_p \tag{19b}$$

$$R_{CG} = \frac{2}{3} \left[\frac{R^2 + RR_I + R_I^{\,2}}{R + R_I} \right] \tag{20a}$$

$$r_{CG} = \frac{2}{3} \left[\frac{R_I^{\,2} + r_p R_I + r_p^{\,2}}{R_I + r_p} \right] \tag{20b}$$

$$V_T = \dot{R}_{CG} \tag{21a}$$

$$V_p = \dot{r}_{CG} \, . \tag{21b}$$

Equilibrium of radial momentum for the moving target and penetrator segments yields the following two equations,

$$\begin{aligned} M_T \, \dot{V}_T = & - R \, H \, (\sigma_T + \rho_{To} \, V_T^{\,2}) \\ & - \mu_T \, V_T \, (R^2 - R_I^{\,2})/H \\ & + R_I \, H \, [\sigma + \rho \, (V_T - V_p)^2] \end{aligned} \tag{22}$$

and

$$M_p \dot{V}_p = - R_I H \left[\sigma_T + \rho_T (V_T - V_p)^2\right] . \qquad (23)$$

We have 10 equations and 11 unknowns. Therefore an additional assumption is needed. Depending upon the penetrator, the authors propose either of the following two; (a) assume $r_p \equiv 0$ and hence the penetrator material is expanding into the hole or, (b) assume $\rho = \rho_o$ and hence the radial shape of the penetrator changes as the hole expands. Based upon either assumption, the location and velocity of the penetrator segment is directly related to the interface location R_I. Assumption (a) relates to R_I via Equations (20b) and (21b), whereas assumption (b) relates to R_I through Equations (18b), (19b), and (21b).

Equations (18) through (21) and either of the above assumptions can be combined with Equations (22) and (23) to yield two coupled differential equations for the unknowns R_I and R. The initial conditions associated with these differential equations come from the solution of Equations (10) through (17), i.e.,

$$\begin{aligned} R\ (t_p + 2t^*) &= R_o^{**} \\ R_I\ (t_p + 2t^*) &= r^{**}\ (t_p + 2t^*) \\ V_T\ (t_p + 2t^*) &= V_{CG}^{**}\ (t_p + 2t^*) \\ V_p\ (t_p + 2t^*) &= \dot{r}_{CG}^{**}\ (t_p + 2t^*). \end{aligned} \qquad (24)$$

III. DISCUSSION

Due to the assumed conversion between axial and radial flows, the axial-flow equations are independent of the radial-flow equations. Therefore, the hierarchy of the solution scheme for the above equations is as follows. First, for the jet, one must solve for the penetration velocity U from Equation (6) (with $dH/dt = d^2H/dt^2 \equiv 0$) with Equations (1) and (8) being used for the jet length ℓ and penetrator velocity, whereas for a rod, Equations (6) and (9) must be solved simultaneously for U and V, with Equations (1) and (5) being used for ℓ and M_I. Once U and V are determined, Equations (14) and (15) can be evaluated in terms of a penetration time t_p, and algebraic Equations (16) and (17) yield the unknown radial boundaries R_o^* and R_o^{**}. With R_o^* and R_o^{**} known, Equations (18) through (24) can be evaluated. Then, Equations (22) and (23) must be solved simultaneously for R and R_I. Note that R_I corresponds to the instantaneous hole profile located at penetration depth P. The solutions for R and R_I depend implicitly upon the time t_p and usage of the known U ($\equiv dP/dt$) permits the corresponding depth of penetration to be calculated. Hence, one obtains the hole growth at

depths of penetration associated with preselected values of t_p.

Because of the non-linearities of the above set of equations, a general closed-form solution for either a rod or jet was not evident to the authors. For axial flow an elaborate integral-differential equation for V is obtained for a KE rod, and a second-order differential equation for P develops for a shaped-charge jet. The second order equation is extremely cumbersome since the radius r is a function of time and the time derivatives of momentum involve $\dot{r}_j(t)$, i.e.,

$$\dot{r}_j(t) = \frac{- r_o V_o}{Z_o[1 + t V_o/Z_o]^{3/2}} = r_o/[t_o(1 + t/t_o)^{3/2}] \qquad (25)$$

where the definitions of ℓ_o and t_o have been substituted into Equation (25). Interestingly, Equation (25) shows that the time variation $\dot{r}(t)$ will be small for the condition of a large value of t_o, i.e., large standoff-distances Z_o or slow velocities V_o. For this condition, the jet's radius can be considered to be approximately constant. This greatly simplifies the conservation equations and enables approximate closed-form solutions to be obtained. In fact, numerical solutions of Equations (6), and (9) are underway using the method of weighted residuals[19].

Whereas the equations for radial target flow (Equations (23) and (24)) are not complicated by the expressions for $\ell(t)$ and $r(t)$, they are second-order with respect to both R and R_I and are extremely non-linear because of the relationships of Equations (20) and (21). Again, no closed-form solution was obvious to the authors. An order-of-magnitude analysis and some special-case solutions are currently being investigated and will be reported at a later date.

For the case of axial flow, special closed-form solutions can be obtained if other assumptions are made. Appendix I gives the axial-momentum equation for a KE penetrator when region II is viewed as a shock interface. Applying the jump conditions[20] to this interface, one obtains a relationship between V and U. Then, assuming a constant-length penetrator, the penetration and center-of-mass velocities are obtained as a function of time for inviscid flow. The influence of viscous effects is shown via an approximate solution.

---

[19] *B. A. Finlayson and L. E. Scriven, "The Method of Weighted Residuals - A Review," Applied Mechanics Reviews, Vol. 19, No. 9, September 1966.*

[20] *N. Cristescu, "Dynamic Plasticity," Chapter VIII, Vol. 4, North-Holland Publishing Company, Amsterdam, 1967.*

Appendix II gives the solution for a steady-state case and one obtains the familiar shaped-charge jet relationships. Also, an order-of-magnitude analysis, based on the assumption that the normalized jet radius is small, reveals that the familiar shaped-charge jet relationships can be obtained without assuming axial steady-state. The order-of-magnitude analysis also shows the relaxation to the Allison-Vitali[4] and DSM[3] shaped-charge jet theories. Appendix III contains the solutions to the special cases of Johnson's KE penetrator[10] and constant velocity penetrators which merely erode during penetration. Appendix IV gives the general solution (with strength and viscosity) to the problem of a non-eroding penetrator which is decelerated by the target, e.g., a steel bullet into sand or clay.

It should be noted that, other than the steady-state solution, all the special solutions exhibit penetration versus time behavior analogous to that observed for a shaped-charge jet (see Figure 7). The data in Figure 7 have been normalized using P_{max} and τ_B, where $t/\tau_B = 1$ corresponds to the approximate time when the jet starts to break up into discrete segments. Note that the penetration proceeds in a continuous fashion throughout the entire time domain. Also, for moderate changes in standoff condition, there appears to be only a slight change in the penetration versus time behavior (see Figure 8). Therefore, even though the model was developed for a continuous jet, it is the authors contention that the model should be applicable to a particulated jet as long as the spacing between jet particles is small compared to the particle lengths. When this is not the case, one can consecutively apply the KE rod equations to each particle in the jet.

In general, all of the solutions yield time-dependent functions. However, maximum penetration P_m can be obtained by evaluating $P(t \rightarrow t_m)$ where t_m is the time where the penetration process stops. The penetration process stops when the penetration velocity U goes to zero. Therefore, by equating the expression for U equal to zero, one can solve for $t_m(1)$. Another value of maximum time $t_m(2)$ can be obtained by equating the penetrator length (Equation (1)) equal to zero. Note that, depending upon target and penetrator conditions, both values of t_m might approach infinity. By comparing these values t_m, insight into the penetration process can be obtained. If $t_m(1) = t_m(2)$, this implies that the penetrator is completely used up during penetration and the penetration process stops when the penetrator is dissipated, i.e., no secondary penetration occurs. If $t_m(1) > t_m(2)$, penetration continues after the penetrator is dissipated and secondary penetration occurs, e.g., hypervelocity impact into a lead target. Lastly, if $t_m(1) < t_m(2)$ the penetration process stops before the penetrator is completely expended, e.g., penetration by a shaped-charge jet, or low velocity impact by a tungsten rod into an aluminum target.

Finally, in Appendices II through IV the various special-case closed-form solutions are compared to the experimental data from References 10 and 12 through 14. In all cases for rods, the agreement

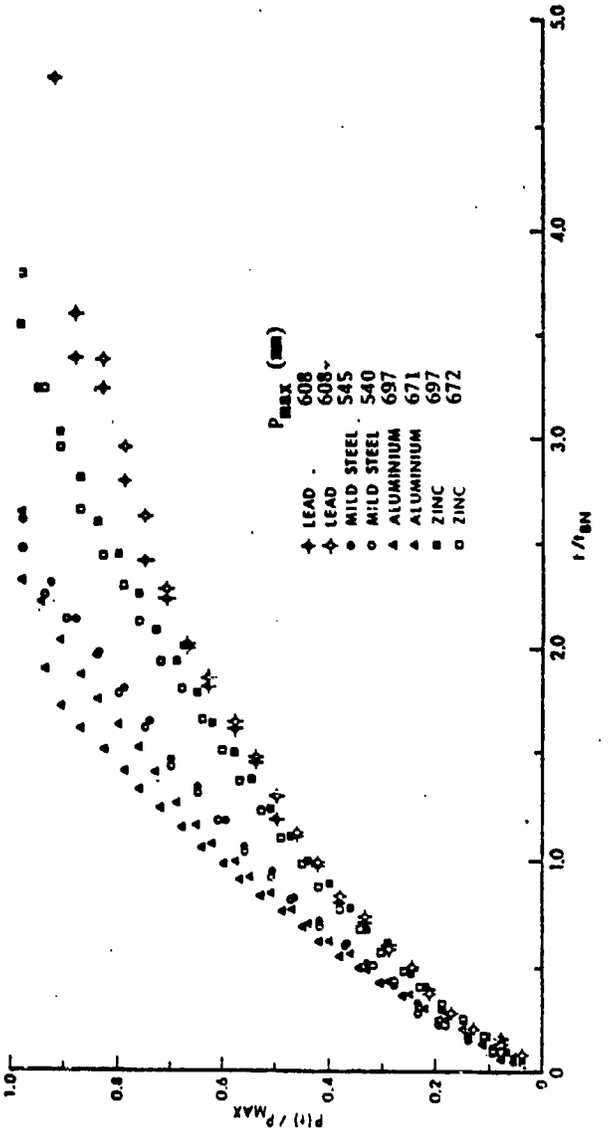

Figure 7. Experimental Penetration versus Time for a Copper Shaped-Charge Jet into Various Target Materials

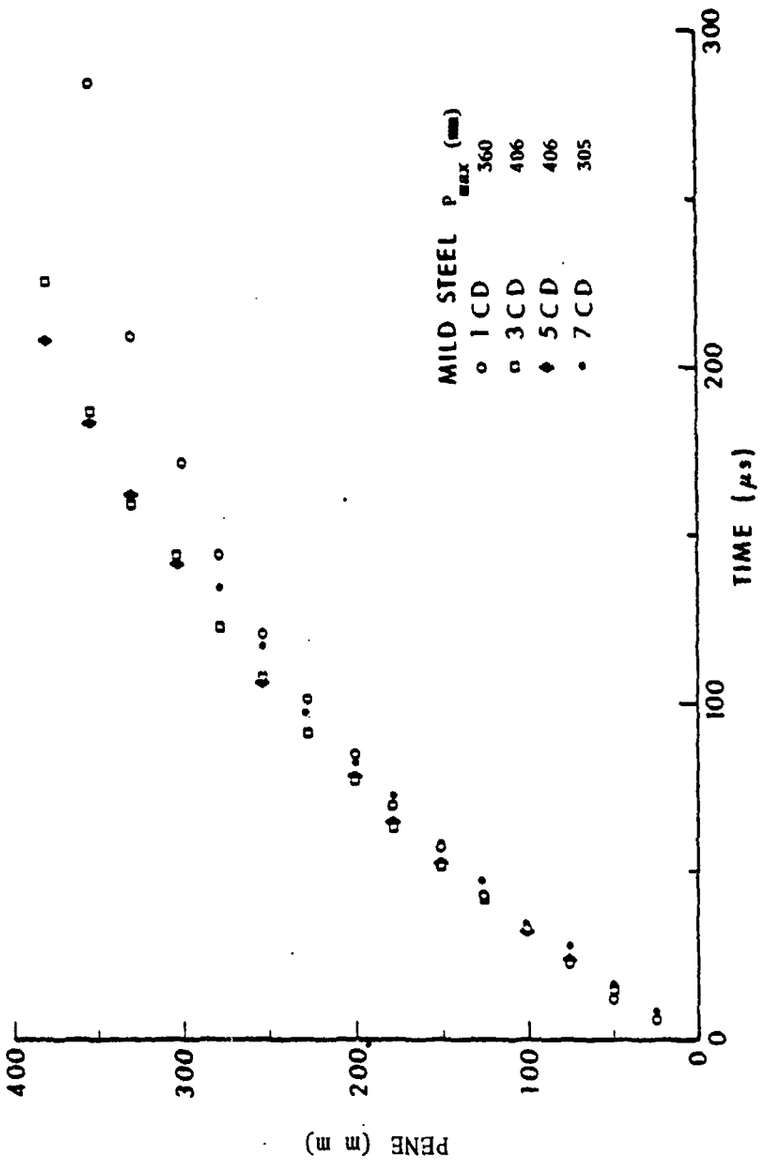

Figure 8. Experimental Penetration versus Time into a Mild Steel Target for Various Shaped-Charge Jet Standoffs

between the special case solutions and the experimental data is good. Note that the values for strength and viscosity were obtained a priori from tabulated values. No attempt was made to curve-fit the data by changing either σ or μ.

For the case of the shaped-charge jets, the authors were interested in showing the effects of various strengths and viscosities upon the predicted results for the approximate models. The approximate models were also judged according to how closely they matched the experimental data. Both the steady-state and the constant-velocity models predict penetrations considerably less than measured when the rod length is set equal to the initial standoff Z_o. If the fully stretched jet-length ($\tau_B(V_o - V_{ro})$) is used, the predicted penetrations are approximately equal to the observed penetrations, except for aluminum. However, using this length gives the erroneous[3,5,6] prediction that the jet's penetration is independent of the standoff distance Z_o. The constant-length model gives results in fair agreement with the experimental results when $\ell_o \equiv Z_o$. This model indicated that, of the four target materials, the penetration calculations for only aluminum and lead were sensitive to the target strength (over the range selected). Conversely, the predicted results for steel are highly dependent upon the viscosity value whereas aluminum is only slightly sensitive to the chosen value. Table IV-1 lists the penetration values discussed above.

IV. SUMMARY AND CONCLUSIONS

A penetration-hole growth model was developed for both KE rods and shaped-charge jet penetrators. This model involves the penetrator, an interaction region located above the target/penetrator interface, and three radial-flow regimes, and includes the effects of stretching jets, material strengths and viscous shear. The interaction region is assumed to form during some small time t* after impact and the axial flow of the target and penetrator materials is assumed to be incompressible. The radial flow of target material is uncoupled from the axial flow of penetrator, i.e., the solution for axial flow (penetration) is independent of the radial flow. Radial flow is assumed to take place in three regimes. First, the target material under the interface flows radially outwards and is compressed (primary flow regime). Next, the eroded penetrator material (due to the velocity difference $V_I - U$) causes additional radial flow and compression of the target material (secondary flow regime). Lastly, the radial target momentum induced during the primary and secondary flow regimes is absorbed by the surrounding target material (tertiary flow regime).

The normalized form of the governing equations for axial flow indicate that the appropriate non-dimensional groups are the density ratio, the Best number, and the Reynolds number. Due to the non-linearity of the equations, the general case must be treated numerically. However, several cases are presented which yield exact solutions.

The first special case is axial steady-state penetration with negligible strength and viscous effects. This case corresponds to the classical shaped-charge jet approach and the model yields both Bernoulli's equation and a maximum penetration which are in agreement with the classical results[1-4].

Also, an order-of-magnitude analysis reveals that Bernoulli's equation represents the dominant order terms in the axial momentum equation when the ordering analysis assumes that the normalized penetrator-radius is small. Also, the Allison-Vitali[4] continuous jet theory follows from the order-of-magnitude analysis.

The second special case considers Johnson's rod penetrator[10] (a penetrator of constant mass). The model's results are analogous to that presented in Reference 10 for inviscid flow and negligible strength effects.

The third special case deals with a uniform velocity penetrator which does not decelerate but does erode away during the penetration process. The predicted penetration appears to follow the general trend of experimental data, i.e., the slope of the penetration versus time behavior is monotonically decreasing. In fact, Figures 9 and 10 indicate good agreement between the theory and the experimental results from Reference 13.

It should be noted that all of the above special cases could be readily extended to allow the penetrator radius to vary with time, and to include both strength and viscous effects.

The last special case considers a rigid rod penetrator which is decelerated by the target but does not erode away. The model shows that the penetrator velocity V must equal the penetration velocity U for this special case. In this case, a closed-form solution is obtained for U(t), penetration P(t), time for penetration $t_m(l)$, and maximum penetration P_m. All of these solutions include the effects of both shear viscosity and material strength. The penetration vs time behavior follows the experimental trends and shows that the slope decreases with increasing target strength and viscosity.

The results of this case (Appendix ..s shown in Figures 11 through 13, where again the agreement with the experimental data from References 14 and 12 is good and Figure 12 matches the trend of the shaped-charge jet data given in Figures 7 and 8.

In summary, it appears that the model is capable of yielding known results for several special cases. These results imply the generality of the model. In addition to predicting P_m, the model predicts (requires an approximate method of solution for the general case) the penetration, penetrator erosion, penetrator mass and velocity, penetration velocity, and radial hole size and growth rate, all as a function of time.

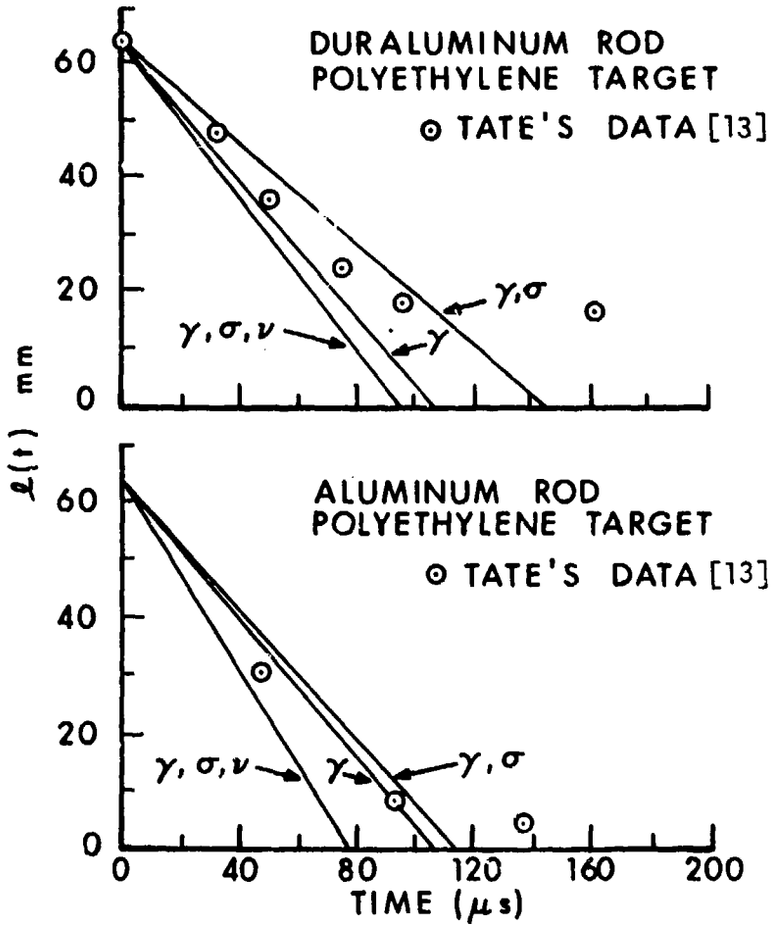

Figure 9. Comparison of the Experimental Rod Erosion Data of [13] with Appendix III Results

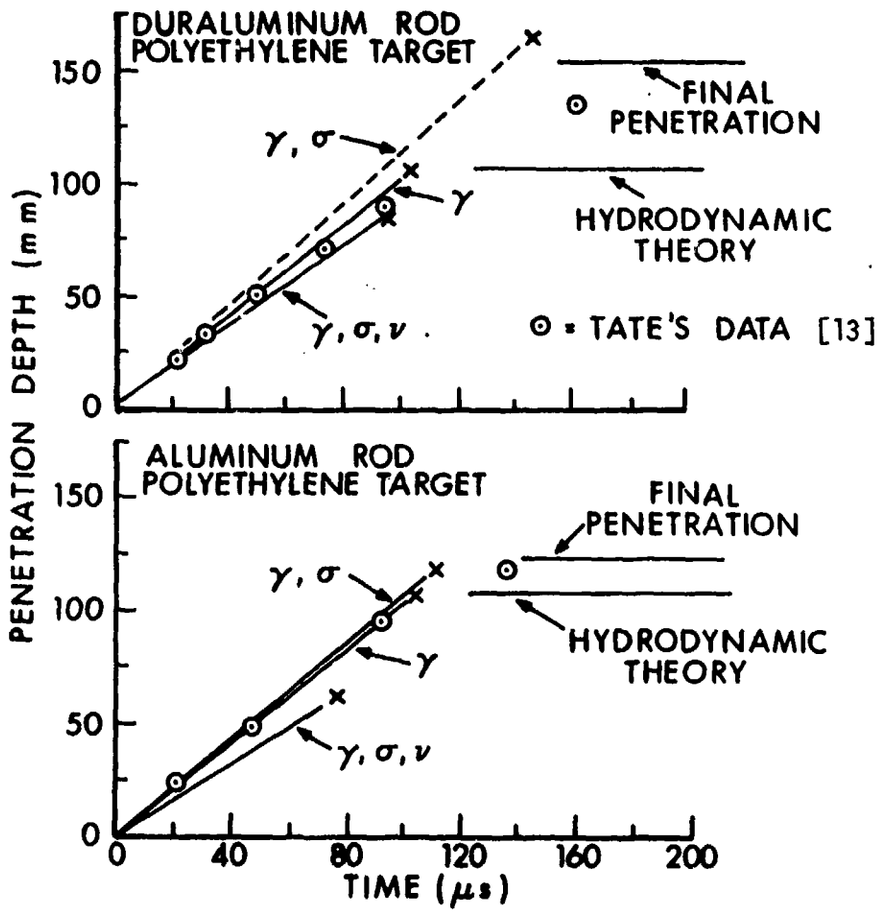

Figure 10. Comparison of the Experimental Penetration Data of [13] with Appendix III Results

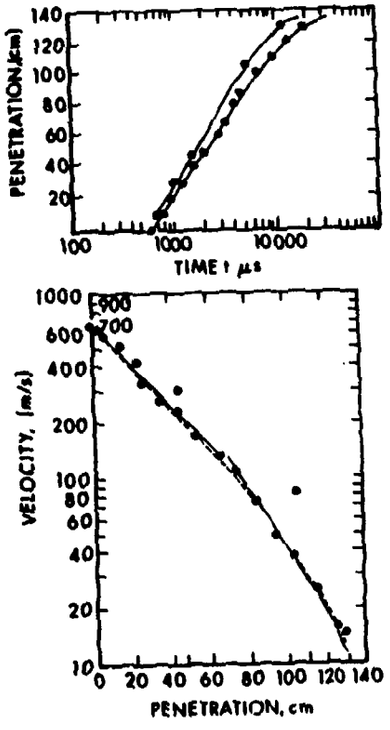

Figure 11. Comparison of the Data from [14] with Appendix IV Results

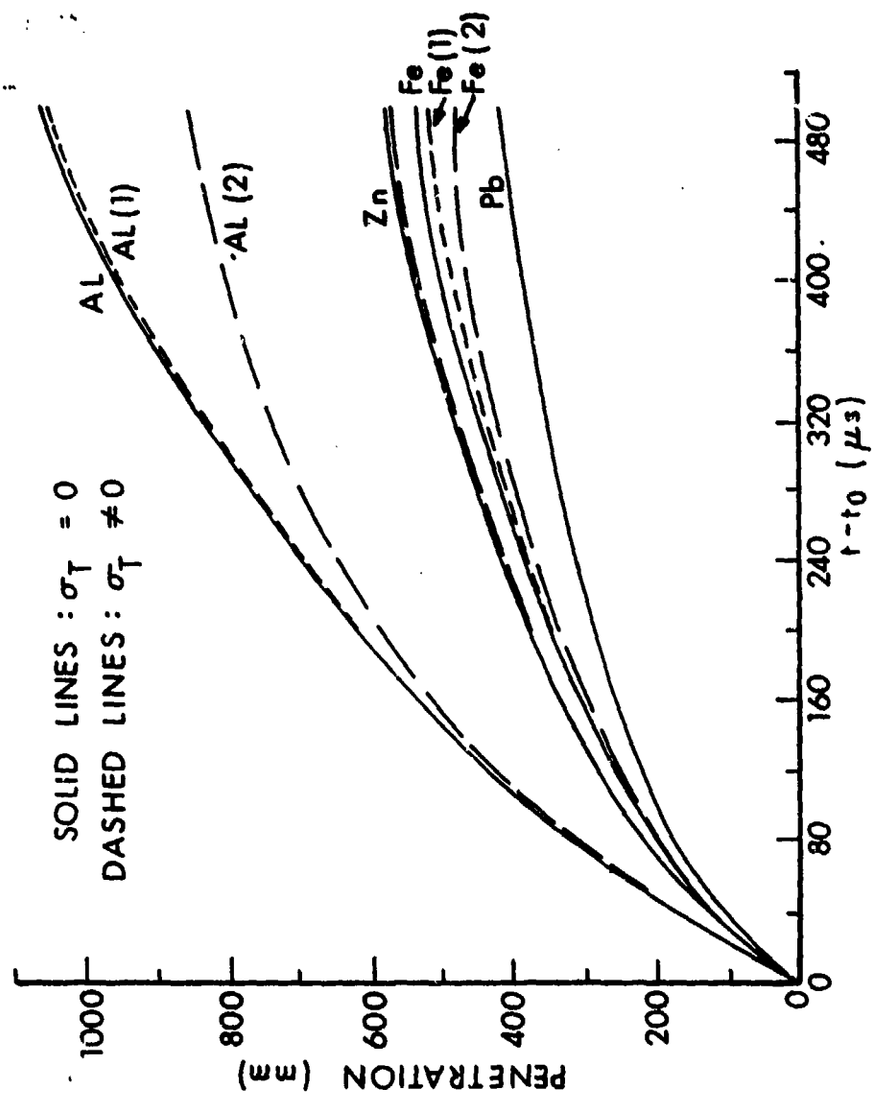

Figure 12. Penetration Results of a Non-eroding Penetrator (Copper) into Various Target Materials from Appendix IV

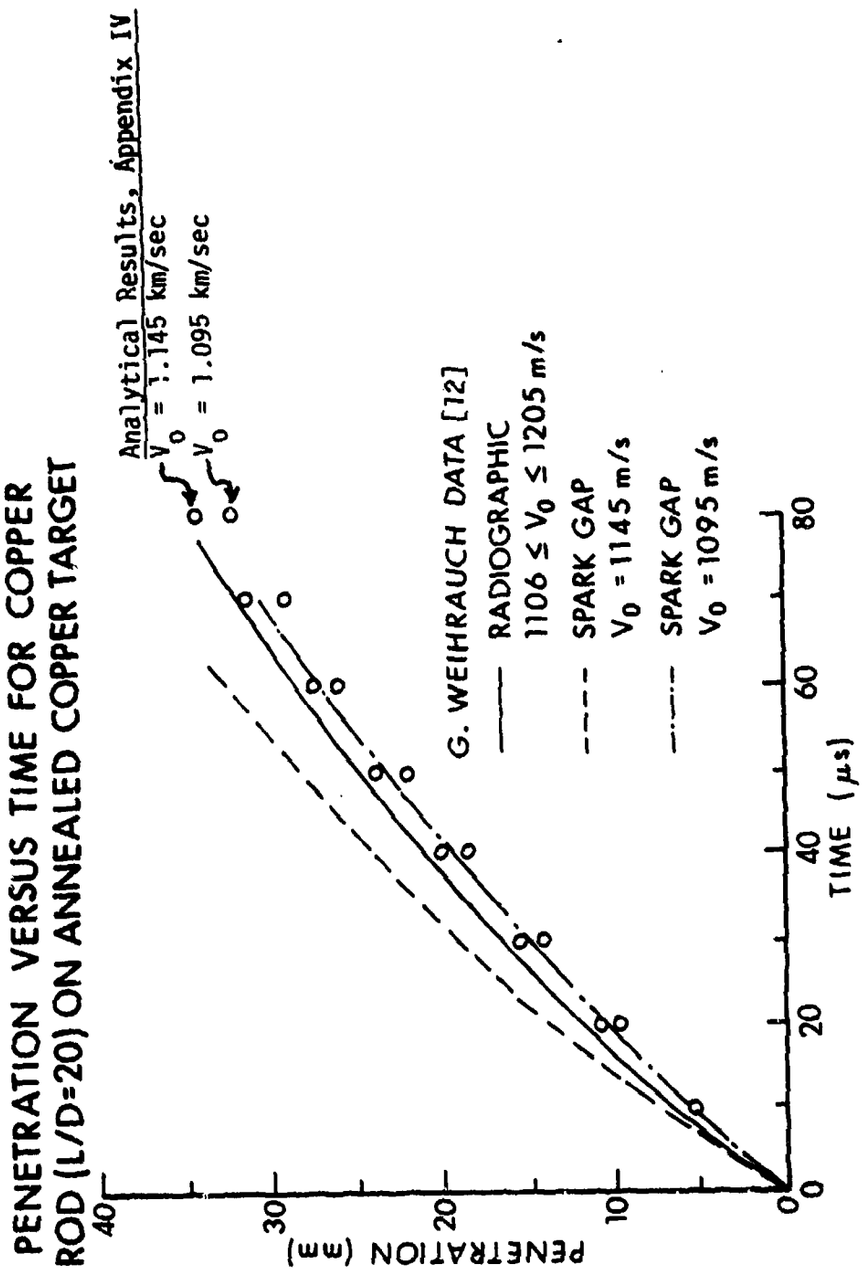

Figure 13. Comparison of the Experimental Penetration Data from [12] with Appendix IV Results

ACKNOWLEDGMENT

The authors wish to thank Mr. A. B. Merendino for the use of the previously unpublished penetration versus time behavior for two 86mm diameter shaped-charges. One charge had a copper liner whose wall thickness was 2.54mm and had an apex angle of 40°, was loaded with Comp B explosive, and had no external body. This data is depicted in Figure 4. Figure 3 presents data from a 42° copper cone, 2.54mm wall, loaded with Comp B explosive, and a thick steel body.

APPENDIX I

AXIAL-MOMENTUM EQUATION FOR A ROD WHEN REGION II IS VIEWED AS A SHOCK INTERFACE

In this approach, the axial-momentum equation is of the following form,

$$\frac{d}{dt}(M_I \, V_{CG}(I)) = \pi r_j^2 (\hat{\sigma}_1 - \hat{\sigma}_2) - \pi \mu P \, V_{CG}(I) \qquad \text{(I-1)}$$

where the difference in surface tractions ($\hat{\sigma}_1$, $\hat{\sigma}_2$) across the shock interface (moving with velocity U with respect to the Eulerian reference) must be obtained from the jump conditions[20]. The flow shear-stresses acting along the embedded length of penetrator is represented by a linearized Newtonian-fluid. The jump conditions associated with continuity and momentum yield the following two equations[20],

$$\hat{\sigma}_1 - \hat{\sigma}_2 = - \rho_1 P_1 \hat{V}_1 + \rho_2 P_2 \hat{V}_2 \qquad \text{(I-2)}$$

$$P_1 \rho_1 = P_2 \rho_2 \qquad \text{(I-3)}$$

where P_1 is velocity of propagation of the interface with respect to particles in region 1 (penetrator), i.e., $P_1 = - U + V_{CG}(I)$, P_2 is the velocity of propagation of the interface with respect to particles in region 2 (target), i.e., $P_2 = U$; $\hat{V}_1$ is the particle velocity in region 1, i.e., $\hat{V}_1 = V_{CG}(I)$; and $\hat{V}_2$ is the particle velocity in region 2, i.e., $\hat{V}_2 = 0$. Therefore, Equations (I-2) and (I-3) become,

$$\hat{\sigma}_1 - \hat{\sigma}_2 = \rho_1 \, V_{CG}(I) \, (U - V_{CG}(I)) \qquad \text{(I-4)}$$

$$\rho_1 \, (V_{CG}(I) - U) = \rho_2 \, U. \qquad \text{(I-5)}$$

Equation (I-5) can be solved for $V_{CG}(I)$ to give,

$$V_{CG}(I) = (1 + \rho_2/\rho_1) \, U \qquad \text{(I-6)}$$

and this relationship and Equation (I-5) substituted into Equation (I-1) yields,

$$\frac{d}{dt}(M_I\, V_{CG}(I)) = -\pi r_j^2\, \rho_2\, V_{CG}^2(I)/(1 + \rho_2/\rho_1) - \pi\, \mu\, P\, V_{CG}(I). \tag{I-7}$$

Note that, if the densities of the target and penetrator materials or either side of the shock are taken to be the initial material densities, then $V_{CG}(I) = [1 + \gamma^2]\, U$ for the shock relationship whereas $V_I = (1 + \gamma)\, U$ for the steady-state jet expression (see Appendix II).

Now, if the rod length is assumed to be <u>constant</u> ($\dot{M}_I = 0$), several approximate solutions can be obtained. First, if the viscous effects in the interaction region are negligible, Equation (I-7) can be solved for $V_{CG}(I)$, i.e.,

$$V_{CG}(I) = \frac{V_o\, \ell_o}{\ell_o + \gamma^2\, V_o(t - t_o)/(1 + \gamma^2)} . \tag{I-8}$$

Equation (I-8) is now substituted into Equation (I-6) and integrated to give the following penetration versus time relationship,

$$P = \frac{\ell_o}{\gamma^2} \ln\, [1 + \gamma^2\, U_o(t - t_o)/\ell_o] . \tag{I-9}$$

Note that there is no finite value of P_{max} associated with this inviscid model.

When the viscosity is not negligible, one can transform (letting $\dot{P} = \lambda(P)$) Equation (I-7) and obtain the following first order equation,

$$Ae^{-P\gamma^2/\ell_o} + B - CP = D\, \dot{P} \tag{I-10}$$

where $A = \gamma^4\, r_o^2\, U_o - \nu\, \ell_o$

$B = \ell_o\, \nu$

$C = \gamma^2\, \nu$

$D = \gamma^4\, r_o^2$

and U_o is the initial interface-velocity (the particle velocity

associated with the striking velocity and the Hugoniot behavior of the target and penetrator materials). An explicit solution of Equation (I-10) was not evident to the authors. However, if the exponential is expanded and the first three terms retained (good approximation if $P\,\gamma^2/\ell_o < 1$), the following differential equation is obtained,

$$A + B - P\left(\frac{A\gamma^2}{\ell_o} + C\right) + P^2\,\frac{A\gamma^4}{2\ell_o{}^2} = D\,\dot{P} \quad . \tag{I-11}$$

Equation (I-11) can be viewed as a quadratic for P_{max} based on the penetration velocity ($\dot{P}$) going to zero. The corresponding solution is,

$$P_{max} = \frac{\ell_o}{\gamma^2}\left[\frac{1 \pm \sqrt{1 - 2A}}{A}\right] \tag{I-12}$$

where $A \equiv (1 - \nu\,\ell_o/r_o{}^2\,\gamma^4\,U_o)$ and Equation (I-12) is subject to the restriction that $P\gamma^2/\ell_o < 1$. Equation (I-12) yields non-imaginary solutions and satisfies the restriction when $A < 0$, i.e.,

$$\nu\,\ell_o > \gamma^4\,r_o{}^2\,U_o \quad . \tag{I-13}$$

Furthermore, since P_{max} must be a positive number, the negative sign in Equation (I-12) must be selected.

Equation (I-11) can also be rearranged to give the following integral equations,

$$\int_o^P \frac{dP}{a + b\,P + C\,P^2} = \frac{t - t_o}{r_o{}^2} \tag{I-14}$$

where $a = r_o{}^2\,U_o$

$b = \gamma^2\,a/\ell_o$

$c = (\gamma^4\,a/\ell_o - \nu)/2\,\ell_o$.

The solution of Equation (I-14) depends upon the sign of

$$q \equiv 4\,ac - b^2 = \frac{r_o^2\,U_o}{\ell_o}\left[\gamma^4\,\frac{r_o^2\,U_o}{\ell_o} - 2\nu\right] .$$

If $q > 0$, one obtains an inverse tangent solution whereas $q < 0$ yields an inverse hyperbolic tangent. However, Equations (I-12) and (I-13) imply that $q < 0$ in order for the restriction to be satisfied. Therefore, only the solution for $q < 0$ will be presented here, i.e.,

$$P = \frac{\ell_o}{\gamma^2 A}\left\{B \tanh\left[B\,\frac{\gamma^2 U_o}{2\,\ell_o}\,(t - t_o) + \tanh^{-1}\,(1/B)\right] - 1\right\} \qquad \text{(I-15)}$$

where $$A = \frac{\nu \ell_o}{\gamma^4\,r_o^2\,U_o} - 1$$

and $$B = \sqrt{\left(\frac{2\nu\,\ell_o}{\gamma^4\,r_o^2\,U_o} - 1\right)} .$$

Note that, because the slope of the tanh function only goes to zero as $t \to \infty$, the maximum penetration given by Equation (I-12) occurs theoretically at $t \to \infty$. However, for practical purposes P is within 1% of P_{max} when the argument has a value of only 2.65. This result is analogous to that obtained by hydrodynamic codes for impact problems, i.e., the penetration velocity becomes extremely small but never reaches zero.

APPENDIX II

AXIAL STEADY-STATE SOLUTION AND ORDER-OF-MAGNITUDE ANALYSIS

In this case we assume that $\dot{V}_I = 0$, $\dot{U} = 0$, and $\ddot{H} = 0$ and Equation (6) yields

$$0 = \pi r_j^2 \left[\sigma + (V_I - U)^2 \rho_o\right] - \pi r_j^2 [\sigma_T + \rho_T U^2] - \mu_T H \pi\, 2U \tag{II-1}$$

and if the usual jet assumptions of negligible strength and viscosity are made, one obtains

$$V_I = (1 + \gamma)U \tag{II-2}$$

where $\gamma = \sqrt{\rho_T/\rho}$. This is the well known shaped-charge jet expression[2-4]. Using the definition of $U = dP/dt$ and the fact that V is a constant (hence not given by Equation 8b) one obtains

$$P = V_I(t - t_o)/(1 + \gamma). \tag{II-3}$$

Equation (1) can now be used with Equation (II-3) to find the time $t_m(2)$ when the penetrator length is consumed, i.e.,

$$t_m(2) - t_o = (1 + \gamma)\ell_o/\gamma V_I \,. \tag{II-4}$$

Substituting Equation (II-4) into (II-3) yields

$$P_{max} = \ell_o/\gamma \tag{II-5}$$

which is the classical jet relationship. Note that $t_m(1)$ is not defined since U is assumed to be a constant.

Bernoulli's equation may also be obtained, without recourse to the steady state assumption, by using a nondimensional form of Equations (6), (1) and (8b),

$$\bar{H}\,\bar{r}_j^{\,2}\,\dot{\bar{U}} + \bar{H}\,\bar{r}_j^{\,2}\,\ddot{\bar{H}}/2 = \bar{r}_j^{\,2}\,[\bar{\sigma} - \bar{\sigma}_T]$$

$$+ \bar{r}_j^{\,2}\left[(\bar{V}_I - \bar{U})^2 - \frac{\rho_{T_o}}{\rho_o}\,\bar{U}^2\right] - \frac{\bar{H}}{Re_T}\,(\bar{V}_I + \bar{U}), \tag{II-6}$$

and

$$\bar{V} = \bar{V}_{ro} + (1 - \bar{V}_{ro}) \left[\frac{1 + \bar{P} - \bar{V}_{ro} (\bar{t} - \bar{t}_o)}{1 + (\bar{t} - \bar{t}_o)(1 - \bar{V}_{ro})} \right], \qquad \text{(II-7)}$$

where the "bar" over each term represents a nondimensional value. These equations were normalized using ℓ_o as the characteristic length, V_o as the characteristic velocity, and ℓ_o/V_o as the characteristic time.

We have introduced the Reynolds number, $Re_T = \frac{\ell_o V_o \rho_o}{\mu_T}$, the normalized strengths (the Best or Metz numbers) $\bar{\sigma} = \sigma/\rho_o V_o^2$ and $\bar{\sigma}_T = \sigma_T/\rho_o V_o^2$ and the density ratio as the appropriate nondimensional groups.

Now we define

$\bar{r}_j = r_j/\ell_o << 1$ or $\bar{r}_j = \Theta^*(m)$ where m is small, $\bar{H} = \Theta(m)$,

$\bar{V}_I = \Theta(1)$, $\bar{U} = \Theta(1)$, $\dot{\bar{U}}$ is of $\Theta(1)$, or less, and for $\ddot{\bar{H}}$ of $\Theta(m)$, or less, we have

$$(\bar{V}_I - \bar{U})^2 - \frac{\rho_{T_o}}{\rho_o} \bar{U}^2 = 0 \qquad \text{(II-8)}$$

ignoring terms of order m^3 or less. In this case ρ_{T_o}/ρ_o is assumed to be of order one, or in general $\frac{\rho_{T_o}}{\rho_o} \bar{U}^2$ is of the same order as $(\bar{V}_I - \bar{U})^2$ since there is no a priori reason to assume otherwise. The Best numbers are assumed to be less than one, i.e., $\Theta(m)$ and the Reynolds number is assumed large, i.e., of $\Theta(\frac{1}{m^2})$.

The equation for $\bar{V}_I$ is not altered by the order-of-magnitude analysis.

**The symbol Θ denotes order-of-magnitude.*

Now for a continuous jet,

$$\ell_o = \frac{Z_o}{V_o}(V_o - V_{ro}) \qquad \text{(II-9)}$$

and $U = \frac{V_I}{1+\gamma}$, $\gamma = \sqrt{\rho_{T_o}/\rho_o}$ via the order-of-magnitude analysis, and

$V_I = \frac{Z_o + P}{t}$ using Equation (II-9), where $t_o = Z_o/V_o$.

Since, $U \equiv \dot{P}$, the above equations can be combined to yield

$$\frac{dP}{dt} = \frac{Z_o + P}{t(1+\gamma)} . \qquad \text{(II-10)}$$

Integration of Equation (II-10), for $P = 0$ at $t = t_o$, yields

$$P = Z_o \left\{ \left(\frac{t}{t_o}\right)^{\frac{1}{1+\gamma}} - 1 \right\} , \qquad \text{(II-11)}$$

which agrees with Allison-Vitali[4] and the DSM[3] continuous jet theory for $t \leq \tau_B$, (the breakup time).

The radial flow equations (18) - (23) are not altered by the order-of-magnitude analysis.

APPENDIX III

A. Johnson's KE Penetrator Model (Ref. 10)

The special case of the KE penetrator of Reference 10, which assumed a constant mass projectile with a given initial velocity, is considered here. Since the mass is assumed constant, Equation (1) implies $\dot{\ell} = 0$ or $U = V_I$.

In this case, Equations (6) and (9), for inviscid flow, yield

$$\rho_o(\ell_o + H)\,\dot{U} = -\sigma_T - \rho_{T_o} U^2 \,. \qquad \text{(III-1)}$$

Changing the independent variable from t to P, since $U = \dot{P}$, and neglecting σ_T, Equation (III-1) gives

$$U = U_o \exp\left(-P/\beta\,(\ell_o + H)\right) \qquad \text{(III-2)}$$

where $\beta = \rho_o/\rho_{T_o}$. Also,

$$P = \beta(\ell_o + H)\,\ell n\left(\frac{U_o}{(\ell_o + H)\beta}\,(t - t_o) + 1\right) \,, \qquad \text{(III-3)}$$

and

$$U = \frac{U_o}{1 + \dfrac{U_o(t - t_o)}{\beta(\ell_o + H)}} \,, \qquad \text{(III-4)}$$

results. Equation (III-2) illustrates the same functional form as given in Reference 10. It is interesting to note that Equation (III-4) is of the same form as that derived in Reference 4 for the penetration velocity of a particulated shaped-charge jet. Furthermore, both the time $t_m(1)$ (penetration velocity goes to zero at this time) and the penetration P go towards infinity for this special case.

Inclusion of the strength effects in these equations yields

$$U\sqrt{\frac{\rho_{T_o}}{\sigma_T}} = \frac{U_o\sqrt{\frac{\rho_{T_o}}{\sigma_T}} - \tan\theta}{1 + U_o\sqrt{\frac{\rho_{T_o}}{\sigma_T}}\tan\theta} \quad , \tag{III-5}$$

and

$$P = \beta(\ell_o + H)\ \ell n\left\{\cos\theta + U_o\sqrt{\frac{\rho_{T_o}}{\sigma_T}}\ \sin\theta\right\}, \tag{III-6}$$

where $\theta = \dfrac{(t - t_o)\sqrt{\rho_T\ \sigma_T}}{\rho_o\ (\ell_o + H)}$. In this case, the time $t_m(1)$ is given by the following equation,

$$t_m(1) - t_o = \frac{\rho_o(\ell_o + H)}{\sqrt{\rho_{T_o}\sigma_T}}\tan^{-1}\left(U_o\sqrt{\frac{\rho_{T_o}}{\sigma_T}}\right), \tag{III-7}$$

and the maximum penetration is finite. If Equation (III-7) is substituted into Equation (III-6), the equation for maximum penetration becomes

$$P_{max} = \frac{\rho_o(\ell_o + H)}{\rho_{T_o}}\ \ell n\left[\frac{\sqrt{\sigma_T/\rho_{T_o}}}{\sqrt{U_o^2 + \sigma_T/\rho_{T_o}}} + U_o^2\sqrt{\frac{\rho_{T_o}}{\sigma_T}}\ \ \frac{1}{\sqrt{U_o^2 + \sigma_T/\rho_{T_o}}}\right] \tag{III-8}$$

B. Penetrator with Constant Velocity

It is also of interest to consider a jet without a velocity gradient; $V_{ro} = V_o = V$, or a constant velocity rod. In this case M_{II} is constant since $r_j(t) = r_o$ from Equation (3), and Equation (6) is of the form

$$\dot{U} = A + BU + CU^2 \tag{III-9}$$

where $A = \frac{\sigma - \sigma_T}{\rho_o H} + \frac{V^2}{H}$, $B = -\frac{\mu_T}{\rho_o r_j^2} - \frac{2V}{H}$, and $C = \frac{1}{H}\left(\frac{\beta - 1}{\beta}\right)$.

Letting $q \equiv 4AC - B^2$, we will first assume $q > o$, and in this case Equation (III-9) yields the following solution,

$$t - t_o = \frac{2}{\sqrt{q}} \left\{ \tan^{-1} \frac{2CU + B}{\sqrt{q}} - \tan^{-1} \frac{2CU_o + B}{\sqrt{q}} \right\}. \tag{III-10}$$

When $q < o$, which is usually the situation since the jet velocity terms dominate the strength and viscosity terms, the solution to Equation (III-9) gives

$$t - t_o = \frac{-2}{\sqrt{-q}} \left\{ \tanh^{-1} \frac{2CU + B}{\sqrt{-q}} - \tanh^{-1} \frac{2CU_o + B}{\sqrt{-q}} \right\}. \tag{III-11}$$

Equation (III-9) represents an analytical derivation of the generalized Poncelet form of the penetration equations which has been assumed by previous investigators[10].

It is noteworthy that when the jet and target are of the same density ($\beta = 1$) Equation (III-9) yields

$$U\left(\frac{\nu}{r_o^2} + \frac{2V}{H}\right) - \frac{V^2}{H} = \left[U_o\left(\frac{\nu}{r_o^2} + \frac{2V}{H}\right) - \frac{V^2}{H}\right] \exp\left[-(t - t_o)\left(\frac{2V}{H} - \frac{\nu}{r_o^2}\right)\right]. \tag{III-12}$$

Thus, $\beta = 1$ may be easily treated as a special case.

For $\beta \neq 1$ either Equation (III-10) or Equation (III-11) can be solved for U. We will illustrate the solution for the case of Equation (III-11) which yields the following penetration velocity,

$$\frac{2\,C\,U + B}{\sqrt{-q}} = (X - \tanh\theta)/1 - X\tanh\theta) \qquad \text{(III-13)}$$

and the corresponding penetration is,

$$2\,C\,P + B\,(t - t_o) = -\,2\,\ell n\,\{\cosh\theta - X\sinh\theta\} \qquad \text{(III-14)}$$

where

$$\theta = \frac{\sqrt{-q}\,(t - t_o)}{2} \quad \text{and} \quad X = \frac{2\,C\,U_o + B}{\sqrt{-q}}\ .$$

The length of the penetrator becomes,

$$\ell = \ell_o - V(t - t_o) - \frac{B(t - t_o)}{2C} - \frac{1}{C}\,\ell n\,\{\cosh\theta - X\sinh\theta\}. \qquad \text{(III-15)}$$

Inspection of Equation (III-13) shows that U remains finite as $t \to \infty$ and hence the penetration given by Equation (III-14) $\to \infty$. In this case, the time $t_m(1) \to \infty$ based upon the penetration velocity U, whereas $t_m(2)$ is finite since $\ell(t) \to o$ at some finite time.

Figures 9 and 10 compare the analytical results with the experimental data of Tate[13] for aluminum and duraluminum rods impacting polyethylene targets. Figure 9 presents the penetrator erosion as a function of time where the analytical model includes either density effects (γ); density and strength effects (γ, σ); or density, strength and viscosity (γ, σ, ν) effects†. The analytical results bracket the experimental data and the agreement is good. In Figure 10, penetration versus time results are presented. The analytical models agree with the experimental data and the predicted final-penetrations for density and strength effects agree very well for both the hard and soft aluminum-penetrators.†† Note that the actual final-penetration for both penetrators exceeds that predicted by the hydrodynamic theory.

†*The strength of aluminum*[13] *is 60 MPa and the strength of duraluminum*[13] *is 300 MPa. Polyethylene was assumed to have a density of 0.92 gm/cm*^{3} *and zero strength*[13]. *The kinematic viscosity of polyethylene was assumed to be (0.5 m*^{2}*/sec), i.e., close to that of lead, since no polyethylene viscosity data could be found.*

††*The shock Hugoniot velocity of 1.1 km/s was used as the initial penetration-velocity* U_o.

APPENDIX IV

A CONSTANT LENGTH (NON-ERODING) ROD PENETRATOR

This Appendix considers another special case, namely that the rod length is constant or from Equation (1) $\dot{\ell} = o$ or $\ell = \ell_o$ and the penetrator velocity is equal to the penetration velocity or $U = V_{CG}(I)$. Hence the rod mass is constant (since $r_j = r_o$).

Equations (6) and (9) may be combined to yield

$$\dot{U} (\ell_o + H) = - [a + bU + CU^2], \qquad \text{(IV-1)}$$

where the viscous effects for region I are assumed to be much less than the viscous effects for region II and where $a = \frac{\sigma_T}{\rho_o}$, $b = \frac{2H \mu_T}{\rho_o r_o^2}$, $c = \frac{\rho_{T_o}}{\rho_o}$ and $q = 4ac - b^2$.[†] Equation (IV-1) has the same functional form as the generalized Poncelet equation which has been used extensively in penetration mechanics studies to curve-fit the experimental data.

Equations (6) and (9) are combined since regions I and II are no longer distinct when $U = V_I$. These two equations provide one equation in U.

Equation (IV-1) can be solved for $q > o$ or $q < o$ as in Appendix III. For $q < o$, i.e., the viscous terms dominate, the penetration velocity is

$$2 Uc + b = \frac{\sqrt{-q}\, A + \sqrt{-q} \tanh \theta}{1 + A \tanh \theta} \qquad \text{(IV-2)}$$

where $\theta = \frac{\sqrt{-q}\, (t - t_o)}{2 (\ell_o + H)}$ and $A = \frac{2 U_o c + b}{\sqrt{-q}}$. When $U = o$ we determine $t_m(1)$ for maximum penetration to be

---

[†] *For inviscid flow, the results of Appendix IV are identical to those of Appendix III-A. Appendix III-A was presented separately in order to compare the Appendix III-A results with Ref. (10).*

$$(t_m(1) - t_o) = \frac{2(\ell_o + H)}{\sqrt{-q}} \tanh^{-1}\left[\frac{\sqrt{-q}\, U_o}{U_o\, b + 2a}\right] , \qquad \text{(IV-3)}$$

and the penetration is given by

$$2P\, c + b\, (t - t_o) = 2\, (\ell_o + H)\, \ell n\, \{\cosh \theta + A \sinh \theta\}. \qquad \text{(IV-4)}$$

The maximum penetration is obtained by substituting Equation (IV-3) into Equation (IV-4).

When $q > o$, i.e., the strength and density terms dominate, we have

$$2\, c\, U + b = \frac{\sqrt{q}\, A - \sqrt{q} \tan \theta}{1 + A \tan \theta} \qquad \text{(IV-5)}$$

where now $\theta = \frac{\sqrt{q}\, (t - t_o)}{2(\ell_o + H)}$ and $A = \frac{2\, U_o\, c + b}{\sqrt{q}}$. The maximum time to penetrate $t_m(1)$ becomes,

$$t_m(1) - t_o = \frac{2\, (\ell_o + H)}{\sqrt{q}} \tan^{-1}\left[\frac{U_o \sqrt{q}}{U_o\, b + 2a}\right] . \qquad \text{(IV-6)}$$

This equation shows that the time to reach maximum penetration increases linearly with penetrator length, and decreases in a non-linear fashion with specific target strength (σ_T/ρ_T). Equation (IV-6) also shows that $t_m(1)$ approaches a limiting value as U_o becomes large. The penetration is

$$P = -\frac{b}{2c}\, (t - t_o) + \frac{(\ell_o + H)}{c}\, \ell n\, \{\cos \theta + A \sin \theta\}. \qquad \text{(IV-7)}$$

Inserting Equation (IV-6) into Equation (IV-7) yields the general expression for maximum penetration.

The analytical results of this Appendix are compared with the results of Reference 14 for a steel bullet impacting dry sand. The penetrator may be realistically assumed to be non-eroding. In this case, Figure 11 shows good agreement between the predicted and experimental penetration versus time, penetration velocity versus time, maximum penetration depth, and time to reach final penetration depth.†

†*The sand density is 1.68 gm/cm^3, the strength of sand is 10^7 Pa, and U_o = 0.671 km/sec was taken for the initial Hugoniot velocity. The density of steel is 7.8 gm/cm^3 and inviscid flow was assumed.*

Figure 12 presents the penetration-time history for a non-eroding copper penetrator impacting aluminum, zinc, steel and lead targets. Aℓ(1) or Fe(1) denotes a lower limit on the target strength whereas Aℓ(2) or Fe(2) denotes the higher strength term for the specified target material. Standard handbook values for the strength terms were utilized. Note that the trend of the data agrees with the experimental results from Figure 7 (after the normalization is removed). However, the non-eroding penetrator model overpredicts the actual penetration-time performance.

Figure 13 compares the analytical results with the data of Reference 12 for a copper rod impacting an annealed copper target. Note that the analytical results agree closely with the various experimental measurements.†

Finally, Table IV-1 summarizes the maximum predicted penetration values for a copper penetrator impacting the noted targets. The analytical results follow from Appendices II, III and IV and the experimental data is from Figure 7. The subscript L denotes the lower limit of the variable in question and a subscript U denotes the upper limit. The standoff is denoted by Z_o and ℓ_{max} represents the maximum length ($\tau_B(V_o - V_{ro})$) of the fully stretched jet. In spite of the various assumptions associated with the different models, the analytical data brackets the experimental results and is of the same order of magnitude. Thus, the authors are optimistic that numerical solutions, which will remove the limiting assumptions, will accurately predict shaped-charge jet penetration and the resulting target response.

†*Inviscid flow was assumed and the initial Hugoniot velocity was used (U_o = 0.57 km/sec).*

Model	Target Material =	Mild Steel	Lead	Zinc	Aluminum
Axial Steady State	$\nu, \sigma = 0, \ell = Z_0$	225mm	186mm	235mm	378mm
	$\nu, \sigma = 0, \ell = \ell_{max}$	707	581	739	1,188
Constant Velocity	$\nu, \sigma = 0$	Same as Axial Steady State			
	$\nu = 0, \sigma = \sigma_L, \ell = Z_0$	224	183	235	377
	$\nu = \nu_{CU}, \sigma = \sigma_L, \ell = Z_0$	169	119	179	224
Constant Mass	$\nu, \sigma = 0, \ell = Z_0$	Approaches Infinity			
	$\nu = 0, \sigma = \sigma_L, \ell = Z_0$	646	939	894	1,776
	$\nu = 0, \sigma = \sigma_U, \ell = Z_0$	501	630	766	873
	$\nu = \nu_U, \sigma = \sigma_L, \ell = Z_0$	266	529	X	1,488
	$\nu = \nu_L, \sigma = \sigma_L, \ell = Z_0$	414	X	X	X
Experimental Values (86mm, Comp B, 40^0 Cu Liner at 2 CD)		546mm	610mm	684mm	684mm

Table IV-1. Maximum Penetration Values Associated with Various Anaiytical Assumptions and Actual Shaped-Charge Jet Data

LIST OF SYMBOLS

H	height of interaction region
ℓ	penetrator length
ℓ_o	initial penetrator length
ΔL	length of penetrator lost during formation of interaction region
ℓ_f	free flight length of penetrator
M	target mass per unit radial segment
M_I	mass of region I associated with penetrator
M_{II}	mass of region II associated with interaction region
M_T	moving mass of target per unit radial segment
M_p	moving mass of eroded penetrator per unit radial segment
P	penetration
P_m or P_{max}	maximum penetration
R	radial location of interface between stationary and moving target material
R_{CG}	radial location of the center-of-mass target material
Re	Reynolds number = $\rho V_o \ell_o / \mu$
R_I	radius of the hole profile at some depth P
r_j	penetrator radius
r_{CG}	radius to center-of-mass of penetrator material within the interaction region
$r_o \equiv r(t_o)$	initial penetrator radius
r_p	inside radius of the eroded penetrator material
t_o	time for penetrator to reach target
t	time

LIST OF SYMBOLS

t_m	time when the penetration process stops
t_p	time for penetration to reach depth P
Δt	small increment of time
t^*	H/U
U	penetration velocity
U_o	initial penetration velocity (shock Hugoniot velocity)
V_I	penetrator velocity at top of interaction region
V_o	penetrator tip velocity
V_r	velocity of rear of penetrator
$V_{CG}(I)$	axial velocity of the center-of-mass of penetrator
V_{CG}	radial velocity of a segment of target mass
ΔV	velocity lost during formation of the interaction region
Z_o	shaped charge standoff
ρ	penetrator density
ρ_T	target density
σ	strength of penetrator
σ_T	target strength
μ	dynamic viscosity of penetrator
μ_T	target dynamic viscosity
ν	kinematic viscosity of penetrator
ν_T	target kinematic viscosity
τ_B	jet break up time
Θ	order-of-magnitude
$\gamma = \sqrt{\rho_T/\rho}$	

LIST OF SYMBOLS

$\beta = \rho/\rho_T$

Other symbols are defined in the text.

A "dot" ($\cdot$) above a term denotes its time derivative

A "bar" ($-$) above a term denotes its normalized value

A single "star" ($*$) above a term denotes variables associated with region III for flow regime A

A double "star" ($**$) above a term denotes variables associated with region IV for flow regime B

DISTRIBUTION LIST

No. of Copies	Organization
12	Commander Defense Documentation Center ATTN: DDC-TCA Cameron Station Alexandria, VA 22314
1	Commander US Army Materiel Development and Readiness Command ATTN: DRCDMD-ST 5001 Eisenhower Avenue Alexandria, VA 22333
1	Commander US Army Aviation Research and Development Command ATTN: DRSAV-E P. O. Box 209 St. Louis, MO 63166
	Director US Army Air Mobility Research and Development Laboratory Ames Research Center Moffett Field, CA 94035
1	Commander US Army Electronics Research and Development Command Technical Support Activity ATTN: DELSD-L Fort Monmouth, NJ 07703
1	Commander US Army Communications Rsch and Development Command ATTN: DRDCO-SGS Fort Monmouth, NJ 07703
1	Commander US Army Missile Research and Development Command ATTN: DRDMI-R Redstone Arsenal, AL 35809
1	Commander US Army Missile Materiel Readiness Command ATTN: DRSMI-AOM Redstone Arsenal, AL 35809
1	Commander US Army Tank Automotive Research & Development Cmd ATTN: DRDTA-UL Warren, MI 48090
7	Commander US Army Armament Research and Development Command ATTN: DRDAR-TSS (2 cys) Mr. T. Stevens Mr. G. Randers-Pehrson Dr. N. Clark Mr. J. Hershkowitz Mr. J. Pearson Dover, NJ 07801
1	Commander US Army Armament Materiel Readiness Command ATTN: DRSAR-LEP-L, Tech Lib Rock Island, IL 61299
2	Commander US Army Materials and Mechanics Research Center ATTN: DRXMR-RF, J. Mescall Tech Lib Watertown, MA 02172
1	Director US Army TRADOC Systems Analysis Activity ATTN: ATAA-SL, Tech Lib White Sands Missile Range NM 88002

DISTRIBUTION LIST

No. of Copies	Organization
1	Assistant Secretary of the Army (R&D) ATTN: Asst for Research Washington, DC 20310
2	HQDA (DAMA-ZA; DAMA-AR) Washington, DC 20310
1	Commander US Army Research Office P. O. Box 12211 Research Triangle Park NC 27709
2	Commander Naval Air Systems Command ATTN: Code AIR-310 Code AIR-350 Washington, DC 20360
1	Commander Naval Ordnance Systems Command ATTN: Code ORD-0332 Washington, DC 20360
2	Chief of Naval Research Department of the Navy ATTN: Code 427 Code 470 Washington, DC 20325
1	Commander Naval Surface Weapons Center ATTN: Code 730, Lib Silver Spring, MD 20910
2	Commander Naval Surface Weapons Center ATTN: Code DG-50 DX-21, Lib Br Dahlgren, VA 22448
2	Commander Naval Weapons Center ATTN: Code 4057 Code 45, Tech Lib China Lake, CA 93555
1	Commander Naval Research Laboratory Washington, DC 20375
1	USAF/AFRDDA Washington, DC 20311
1	AFSC/SDW Andrews AFB Washington, DC 20311
1	US Air Force Academy ATTN: Code FJS-41 (NC) Tech Lib Colorado Springs, CO 80840
1	AFATL/DLJW (J. Foster) Eglin AFB, FL 32542
1	AFWL (SUL, LT Tennant) Kirtland AFB, NM 87116
1	AFLC/MMWMC Wright-Patterson AFB, OH 45433
1	AFAL/AVW Wright-Patterson AFB, OH 45433
6	Director Lawrence Livermore Laboratory ATTN: Dr. J. Kury Dr. M. Wilkins Dr. E. Lee Dr. H. Horning Dr. J. Knowles Tech Lib P. O. Box 808 Los Alamos, NM 87544

DISTRIBUTION LIST

No. of Copies	Organization
1	Battelle-Columbus Laboratories ATTN: Mr. Joseph E. Backofen 505 King Avenue Columbus, OH 43201
2	Dyna East Corporation ATTN: P. C. Chou J. Carleone 227 Hemlock Road Wynnewood, PA 19096
1	Honeywell, Inc. Government and Aeronautical Products Division ATTN: C. R. Hargreaves 600 Second Street Hopkins, MN 55343
1	Physics International Corp ATTN: Dr. L. Behrmann 2700 Merced Street San Leandro, CA 94577
1	Sandia Laboratories ATTN: Dr. W. Herrmann Albuquerque, NM 87115
1	Shock Hydrodynamics ATTN: Dr. L. Zernow 4710-4716 Vineland Avenue North Hollywood, CA 91602
1	Systems, Science & Software ATTN: Dr. R. Sedgwick P. O. Box 1620 La Jolla, CA 92037
1	Drexel Institute of Technology Wave Propagation Research Center ATTN: Prof. P. Chou Philadelphia, PA 19104
2	University of California Los Alamos Scientific Lab ATTN: Dr. J. Walsh Tech Lib P. O. Box 1663 Los Alamos, NM 87544
1	University of Denver Denver Research Institute ATTN: Mr. R. F. Recht 2390 S. University Boulevard Denver, CO 80210

Aberdeen Proving Ground

Dir, USAMSAA
ATTN: Dr. J. Sperrazza
B. Oeheli
G. Johnson
Cdr, USATECOM
ATTN: DRSTE-SG-H